

Article

Mineral Chemistry of the Lower Cretaceous Jinling Iron Skarn Deposit, Western Shandong Province, North China Craton: Implications for the Iron Skarn Mineralization Process

Fang-Hua Cui ^{1,2}, Chao Zhang ^{1,2,*}, Dai-Tian Jin ³, Lu-Yuan Wang ^{1,4}, Ji-Lei Gao ^{2,5}, Ming Ma ^{2,5} and Ya-Dong Li ^{2,5}¹ School of Resources and Environmental Engineering, Shandong University of Technology, Zibo 255000, China² Shandong Engineering Laboratory for High-Grade Iron Ore Exploration and Mineral Resources of Shandong Province, Jinan 250100, China³ Downhole Service Company of XDEC (Reservoir Stimulation R&D Center), Karamay 834000, China⁴ Key Laboratory of Mineral Resources Evaluation in Northeast Asia, Ministry of Land and Resources, Changchun 130061, China⁵ No. 1 Institute of Geology and Mineral Resources of Shandong Province, Jinan 255014, China

* Correspondence: czhang@sdut.edu.cn

Abstract: The source of iron material and the mineralization process of iron skarn deposits within the eastern North China Craton are ambiguous. In this study, we present new mineral chemical data of the Jinling skarn deposit, located in western Shandong Province, east China. Based on the petrography study and mineral chemical data, we suggest that the Jinling iron skarn deposit is hydrothermal and the metallogenic iron is enriched by leaching of Fe-rich fluids derived from primitive magmatic melt from the solidified diorites. The Jinling iron skarn deposit formed as a result of several mineralization processes: (1) Fe-rich hydrothermal fluids exsolved from a hydrous parental magma that was characterized by high iron content, oxygen fugacity (fO_2), and salinity; (2) the Fe content of the fluids was augmented during the alkali metasomatism stage via the leaching of Fe from the solidified dioritic rocks; (3) diopside and garnet in skarns formed under relatively alkaline and oxidizing conditions during the later prograde skarn stage; (4) during the retrograde skarn stage, amphibole, chlorite, epidote, phlogopite, serpentine, biotite, and chlorite formed under more oxidizing conditions, and subsequent mixing of the Fe-rich fluids with meteoric water triggered the precipitation of the massive magnetite; and (5) the final sulfide–carbonate stage was involved in the formation of carbonate and sulfide minerals as a result of a change in conditions from oxidizing to reducing.

Keywords: skarn minerals; redox condition; mineralizing fluids; hydrothermalism; source of ore material



Citation: Cui, F.-H.; Zhang, C.; Jin, D.-T.; Wang, L.-Y.; Gao, J.-L.; Ma, M.; Li, Y.-D. Mineral Chemistry of the Lower Cretaceous Jinling Iron Skarn Deposit, Western Shandong Province, North China Craton: Implications for the Iron Skarn Mineralization Process. *Minerals* **2022**, *12*, 1152. <https://doi.org/10.3390/min12091152>

Academic Editor: Jan Marten Huizenga

Received: 25 July 2022

Accepted: 1 September 2022

Published: 12 September 2022

Publisher's Note: MDPI stays neutral with regard to jurisdictional claims in published maps and institutional affiliations.



Copyright: © 2022 by the authors. Licensee MDPI, Basel, Switzerland. This article is an open access article distributed under the terms and conditions of the Creative Commons Attribution (CC BY) license (<https://creativecommons.org/licenses/by/4.0/>).

1. Introduction

Iron plays an important role from both an economic and geological perspective, so it is necessary to carry out innovative research on iron ore-forming theory. There are various iron deposits, consisting of magmatic, structural, sedimentary, and metamorphic units [1]. Iron deposits may have a different genesis, such as skarn iron deposits (magmatic type), which are commonly related to hydrothermal metasomatism [2], while marine ooidal ironstones (sedimentary type) have hydrothermal and/or biogenic origin [3,4]. Iron skarn deposits are a significant source of high-grade iron ores in China. These deposits are distributed along downthrown fault-controlled belts in southwestern Hebei, northeastern Henan, southeastern Shanxi, Subei, Wanbei, and western Shandong in the North China Craton (NCC) (Figure 1). These deposits are hosted at the contact between Paleozoic carbonate rocks and Mesozoic plutonic rocks [2]. Isotope geochronological data measured for skarn and hydrothermal minerals (such as sphene, zircon, and allanite) formed contemporaneously with mineralization in these skarn deposits in eastern North China Craton

show consistent ages that constrain the time of ore formation to 137–127 Ma [5–8]. Two models have been proposed to explain the genesis of these iron skarn deposits: (1) Fe enrichment by the exsolution of Fe-rich fluids from the evolving silicate melt, followed by enrichment of Fe resulting from alkali metasomatism of the shallow plutons [9–12]; and (2) Fe enrichment of hydrothermal fluid by leaching from solidified plutons and/or sedimentary wall rocks, with magnetite precipitation occurring as a result of changes in the physicochemical conditions of the fluid [13]. Studies of skarn ore magnetite have proposed various genetic models of these iron skarn deposits, including ore-forming magma injection and magmatic–hydrothermal mineralization [14,15]. Although the ore-forming stages have been discussed in existing research, the mineralization process and variation of metallogenic conditions in the different ore-forming stages of these iron skarn deposits need to be depicted in detail.

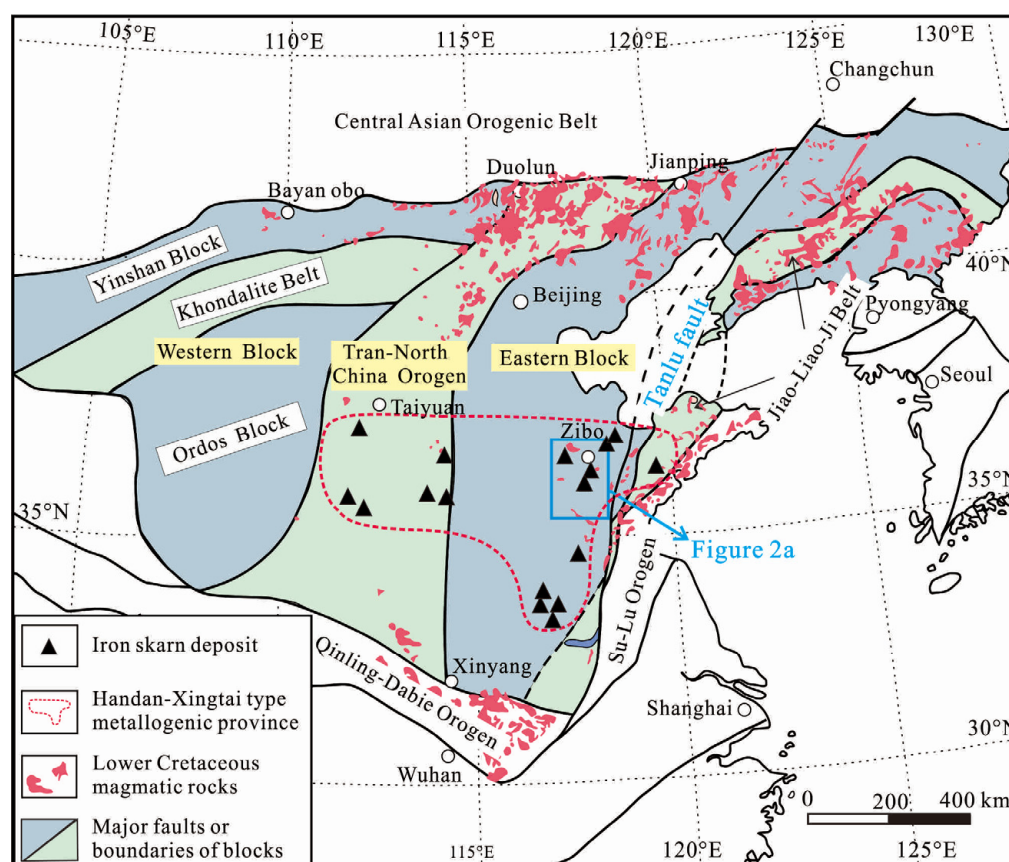


Figure 1. Tectonic sketch map of the North China Craton (modified from Zhao [16]), and distribution of iron skarn deposits (modified from Zhao et al. [2]) and Lower Cretaceous magmatic rocks (modified from Zhang et al. [17]).

Accordingly, the source of iron material, the mineralization process, and the link between magmatism and mineralization in these iron skarn deposits within the eastern North China Craton (NCC) remain ambiguous. The Jinling deposit is one of the largest iron skarn deposits in western Shandong Province, China. This study presents new mineral chemical data for feldspar, amphibole, garnet, clinopyroxene, and magnetite from the Jinling pluton and iron skarn deposit. These results provide mineralogical insights into the mineralization process and metallogenic conditions of iron skarn deposits within the NCC.

2. Geological Background and Sample Description

2.1. Regional Geology

The NCC is one of the world's oldest cratons and underwent large-scale changes as a result of the amalgamation of the Western and Eastern blocks along the Trans–North

China Orogen during the Paleoproterozoic [18,19] (Figure 1) and continuing through to the destruction of these blocks during the late Mesozoic. The basement of the NCC comprises mainly Archean to Paleoproterozoic tonalite–trondhjemite–granodiorite (TTG) gneiss that underwent amphibolite- to granulite-facies metamorphism and was subsequently unconformably overlain by Mesoproterozoic to Cenozoic cover successions [20,21]. Western Shandong is located in the southeastern NCC and is bounded to the east by the trans-lithospheric Tan–Lu Fault (Figure 2a). Sedimentary rocks in the area are dominated by Paleozoic carbonates and clastic rocks. Mesozoic magmatic rocks intruded the Precambrian basement rocks and sedimentary strata from the Late Triassic (~225 Ma) to the Late Cretaceous (~73 Ma), with a peak during the Early Cretaceous (132–112 Ma) [17]. Structural features in western Shandong comprise folds and ductile shear belts in the Precambrian basement, synclines and brachyanticlines in the Paleozoic strata, and NW- to NNE-trending faults. Mesozoic mineralization and magmatic activity were associated with faults that formed as a result of the reactivation of the Tan–Lu Fault.

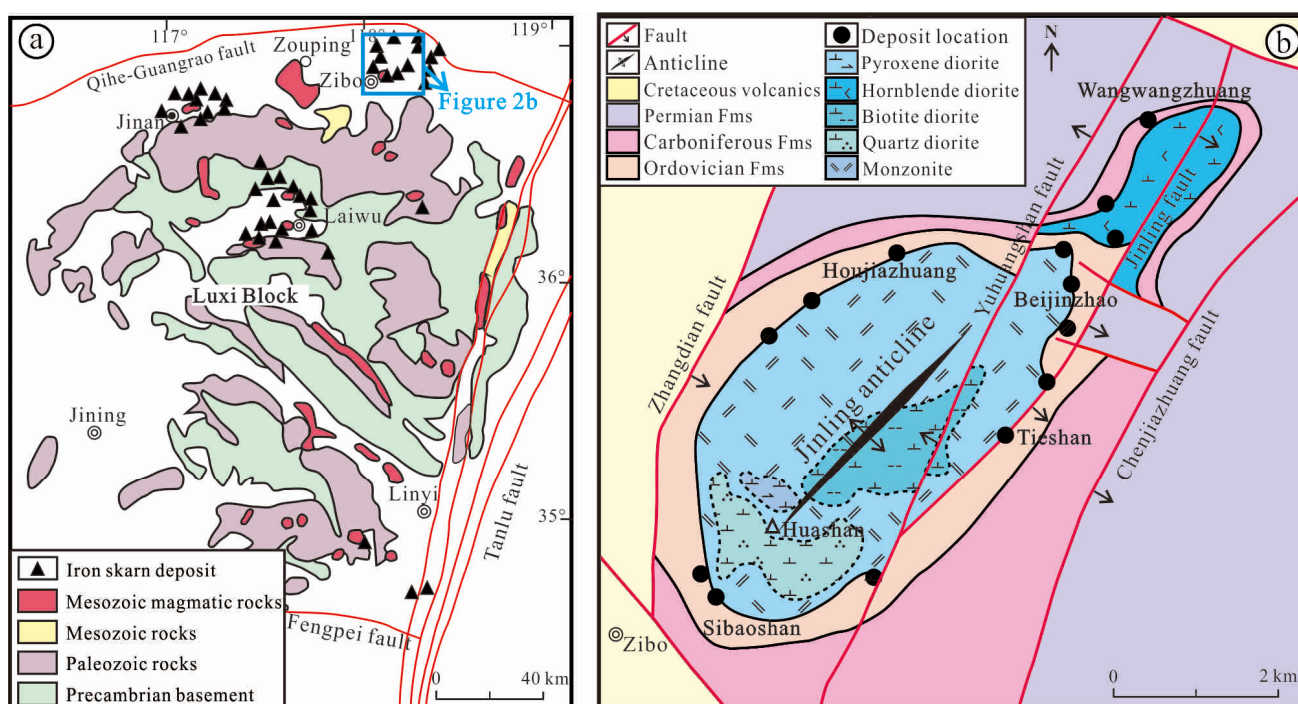


Figure 2. (a) Simplified geological map of western Shandong (modified from Lan et al. [22]). (b) Sketch map of the Jinling pluton and distribution of the Jinling iron skarn deposits (modified from Hao [23]).

2.2. Geology of the Jinling Iron Skarn Deposit

The Jinling typical iron skarn deposit of the NCC is associated with dioritic plutons and Paleozoic carbonates. It occurs in the Jinling brachyanticline, with the hosted iron ore bodies being distributed along its periphery (Figure 2b). The core of the brachyanticline comprises the ore-related Jinling pluton, which is composed predominantly of basic–intermediate diorites, weakly alkaline diorites, and dike rocks [23].

Fourteen ore bodies have been identified in the Houjiazhuang and Wangwangzhuang areas. The lenticular to stratoid ore bodies are distributed along the contact zone and range in thickness from 2.5 to 25.0 m (Figure 3). These ores are characterized by Fe grades of >51 wt.% and associated with copper, cobalt, and other components. The ore bodies of the Jinling iron skarn deposit are located at the contact between the Mesozoic dioritic rocks and the Ordovician Majiagou Formation carbonates. Three alteration or metamorphic zones have been identified (from the center of the pluton to the wall rocks): the alkali alteration zone, the contact metamorphic zone (the skarn zone), and the thermal contact metamorphic

zone. The alkali (sodic) alteration zone is restricted to the dioritic rocks. The wall rocks were metamorphosed to recrystallized limestone and marble in the thermal contact metamorphic zone (Figure 4). Skarn formation resulted from the intense metasomatism that occurred at the contact between the diorites and carbonates (i.e., in the contact metamorphic zone). As a result, the ore bodies are distributed close to the wall rocks within the skarn zone (Figure 3) and mainly consist of magnetite with minor minerals, such as diopside, garnet, epidote, amphibole, chlorite, calcite, chalcopyrite, and pyrite.

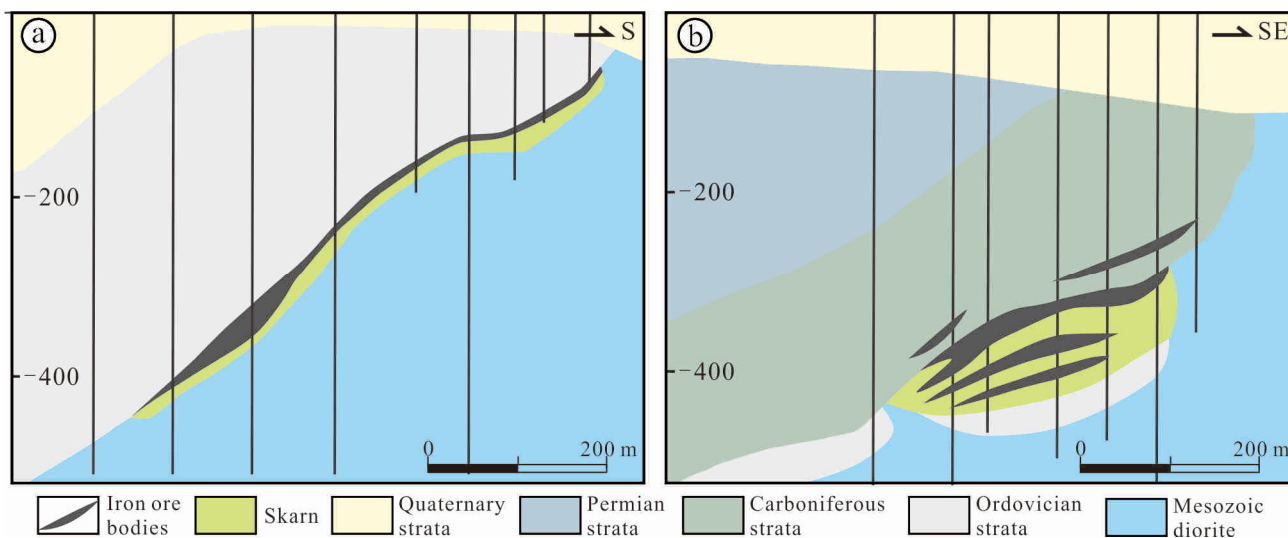


Figure 3. Cross-section diagram of the Jinling iron deposit (modified from Hao [23]). (a) Houjiazhuang ore section. (b) Wangwangzhuang ore section.

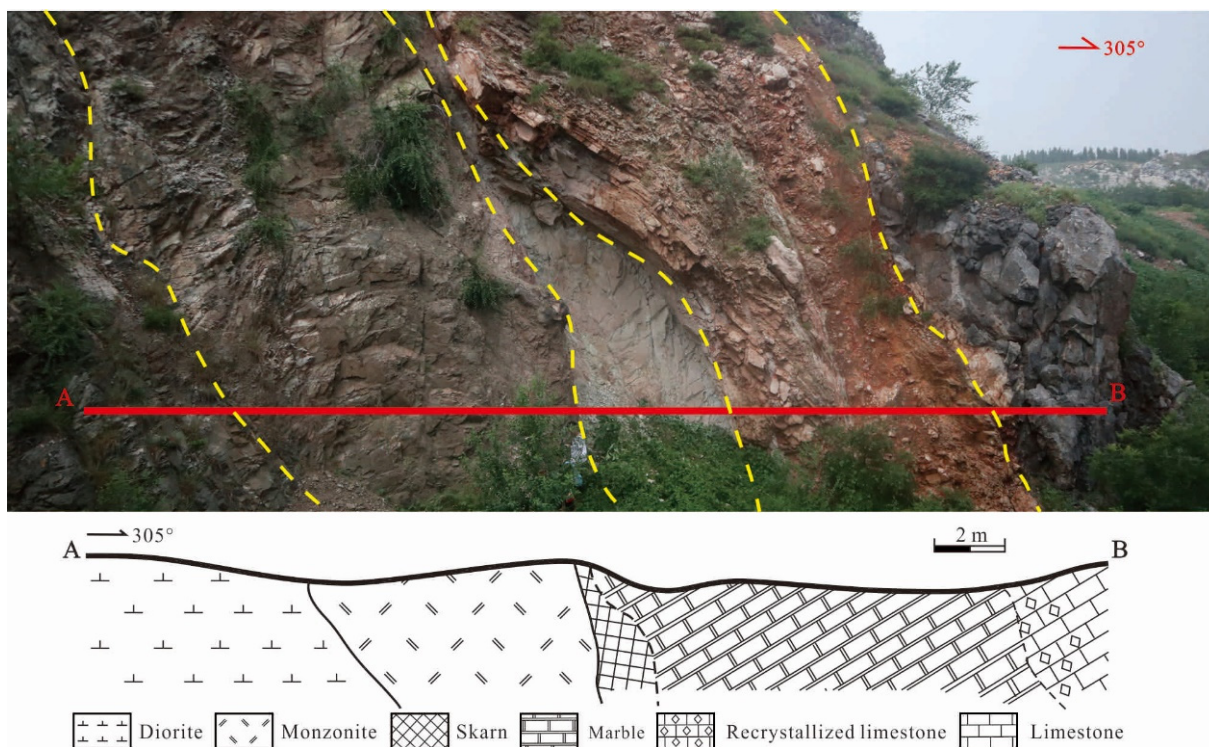


Figure 4. Schematic section view of the contact zone between the Jinling dioritic pluton and Ordovician carbonates, including marble, recrystallized limestone, and limestone. The yellow dashed line in this figure is the boundary of geological bodies.

3. Petrography

3.1. Jinling Ore-Related Pluton

The Jinling ore-related pluton occurs within Ordovician limestone in the core of the Jinling brachyanticline (Figure 2b). The lithology of this pluton is complex, comprising pyroxene diorite, hornblende diorite, biotite diorite, quartz diorite, and monzonite. This complexity arises from the multiple pulses of magma that formed the pluton [23]. Their distribution is illustrated in Figure 2b. Alkali metasomatism, particularly sodic alteration, is common in these rocks (Figure 5a–c). Although most of the Jinling iron ore bodies occur at the contact between monzonite and Ordovician limestone, some are found at the contact between hornblende diorite and Carboniferous rocks (Figure 2b).

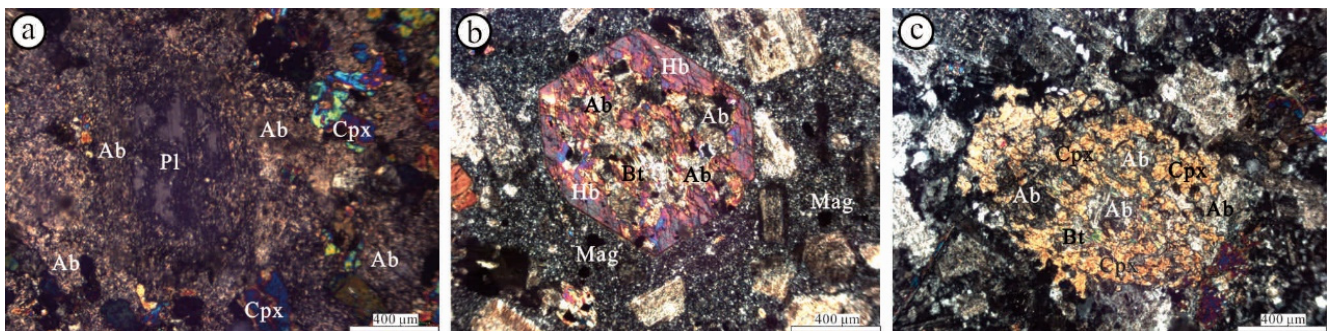


Figure 5. Petrographic features of plutonic rocks of the Jinling pluton. (a) Intensely albitized diorites show the replacement of plagioclase by albite. (b,c) Small albite and biotite grains have partially replaced hornblende and pyroxene resulting from alkali metasomatism. All photos were taken under crossed polarizers. Abbreviations: Ab = albite, Hb = hornblende, Bt = biotite, Cpx = clinopyroxene, Mag = magnetite, Pl = plagioclase.

3.2. Skarn and Iron Ore of the Jinling Deposit

The skarn and iron ore bodies in the Jinling deposit are the product of intense metasomatism (Figure 3). The skarn, which is 0.5–30.0 m thick, is developed at the base of the ore bodies (Figure 3) and is composed of garnet, diopside, epidote, amphibole, phlogopite, chlorite, serpentine, and calcite.

Three types of iron ore occur in the Jinling deposit: massive, banded, and disseminated. Massive ore is the dominant type, whereas disseminated and banded iron ores are less common. Massive iron ore comprises >80 wt.% subhedral to euhedral magnetites of 0.1 to 5.0 mm in size. Massive magnetites characterized by smaller grain sizes coexist with biotite, chlorite, and serpentine (Figure 6b,c,f,h), whereas those characterized by larger grain sizes coexist with altered diopside, garnet, and calcite (Figure 6g,i,j). Disseminated iron ore occurs mainly in fractures within altered plutonic rocks and skarn, and comprises <50 wt.% subhedral–granular magnetites of 0.01 to 0.20 mm in size (Figure 6a). Banded iron ore occurs along two sides of the massive ores. The iron-rich bands are 0.05 to 0.20 mm thick and contain ~60 wt.% magnetite (Figure 6d). Many of the magnetite grains in the banded ores have enclosed early anhedral and metasomatized diopside (Figure 6e). A small amount of euhedral pyrite and chalcopyrite occur as veins that cut the massive ores locally (Figure 6k,l).

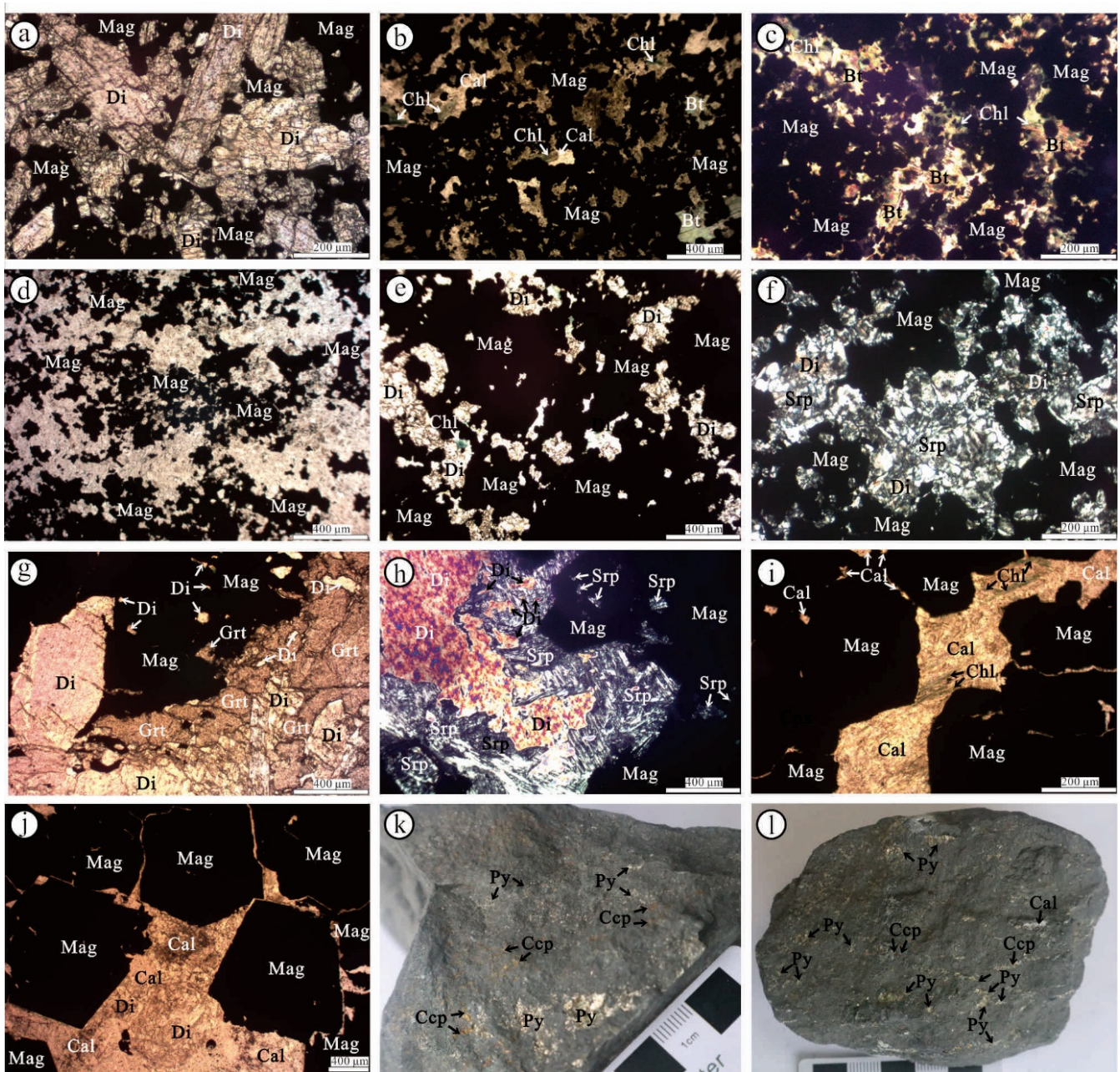


Figure 6. Various types of iron ore and characteristics of wall rocks in the Jinling iron skarn deposit. (a) Disseminated magnetite that is interstitial to early euhedral diopside. (b,c) Massive magnetite crystals coexisted with biotite and chlorite. (d) Banded magnetite. (e) Banded magnetite that has enclosed an early anhedral crystal of diopside that was metasomatized. (f) Massive magnetite crystals coexisted with fibrous serpentine that has completely replaced early diopside. (g) Metasomatic texture formed between early subhedral–euhedral diopside, garnet, and late massive magnetite. (h) The residual metasomatic texture between diopside and fibrous serpentine coexisted with massive magnetite. (i,j) Late calcite has partially replaced euhedral massive magnetite. (k,l) Euhedral pyrite and chalcopyrite veins in iron ore. Photos (a,b,d,e,g,i,j) were taken under open polarizers and (c,f,h) taken under crossed polarizers. Abbreviations: Bt = biotite, Cal = calcite, Chl = chlorite, Ccp = chalcopyrite, Di = diopside, Grt = garnet, Mag = magnetite, Py = pyrite, Srp = serpentine.

3.3. Mineral Paragenetic Sequence

Based on field mapping and petrography, the mineralization in the Jinling deposit can be divided into four stages: (i) alkali metasomatism, (ii) prograde skarn, (iii) retrograde skarn, and (iv) sulfide–carbonate.

During the alkali metasomatism stage, plagioclase, amphibole, and pyroxene in the diorites were partially replaced by small subhedral–euhedral albite and biotite grains (Figure 5a–c).

The minerals that formed during the prograde skarn stage comprise diopside–garnet \pm disseminated and banded magnetite. Two types of diopside are recognized based on color: colorless and light green (Figure 7a). The colorless diopsides formed first and have been partially replaced by garnet and magnetite (Figure 6g), whereas the light-green diopsides formed later along the margins of the colorless variety and coexist with subhedral garnet (Figure 7a). The diopsides have been intensely altered and partially replaced by amphibole, epidote, biotite, and quartz (Figure 7b–g). Zoned andradite and the colorless diopside have been partially replaced by later massive magnetite (Figures 6g and 7h,i). Disseminated and banded magnetite grains that formed during the prograde skarn stage are subhedral–anhedral, occur interstitial to diopside (Figure 6a,e), and constitute 50 wt.%–70 wt.% of the rock.

The minerals that formed during the retrograde skarn stage comprise amphibole–epidote, phlogopite, serpentine, biotite, chlorite, and massive magnetite. Amphibole is divided into two compositional types. Alkali amphiboles coexist with massive magnetite and occur as needle-shaped to fibrous aggregates (Figures 6b,c and 7j). Ca-rich amphiboles occur as subhedral–euhedral crystals, coexist with phlogopite and epidote, and are partially replaced by late pyrite and calcite (Figure 7b,c,e). The subhedral–euhedral epidote coexisting with Ca-rich amphibole has partially replaced the early diopside (Figure 7c,d), and replacement relict textures between serpentine and diopside have also been preserved (Figure 6f,h). In contrast, the fine-grained euhedral phlogopite, serpentine, and biotite that coexist with massive magnetite occur interstitially to the early diopside (Figures 6b,c and 7f,g). Subhedral–euhedral massive magnetites that coexist with alkali amphibole, biotite, chlorite, and serpentine (Figure 6b,c,f,h) have locally modified early diopside and garnet (Figure 7i).

The minerals that formed during the sulfide–carbonate stage comprise calcite, quartz, pyrite, and chalcopyrite. Anhedral calcite and quartz are the predominant minerals and occur interstitially to skarn minerals (Figures 6i,j and 7a,b,d,f,i–l). Euhedral pyrite associated with anhedral calcite occurs interstitially to diopside and Ca-rich amphibole (Figure 7e,l). Euhedral pyrite and chalcopyrite also occur in veins that cut the ore (Figure 6k,l).

The mineral paragenetic sequence is illustrated in Figure 8.

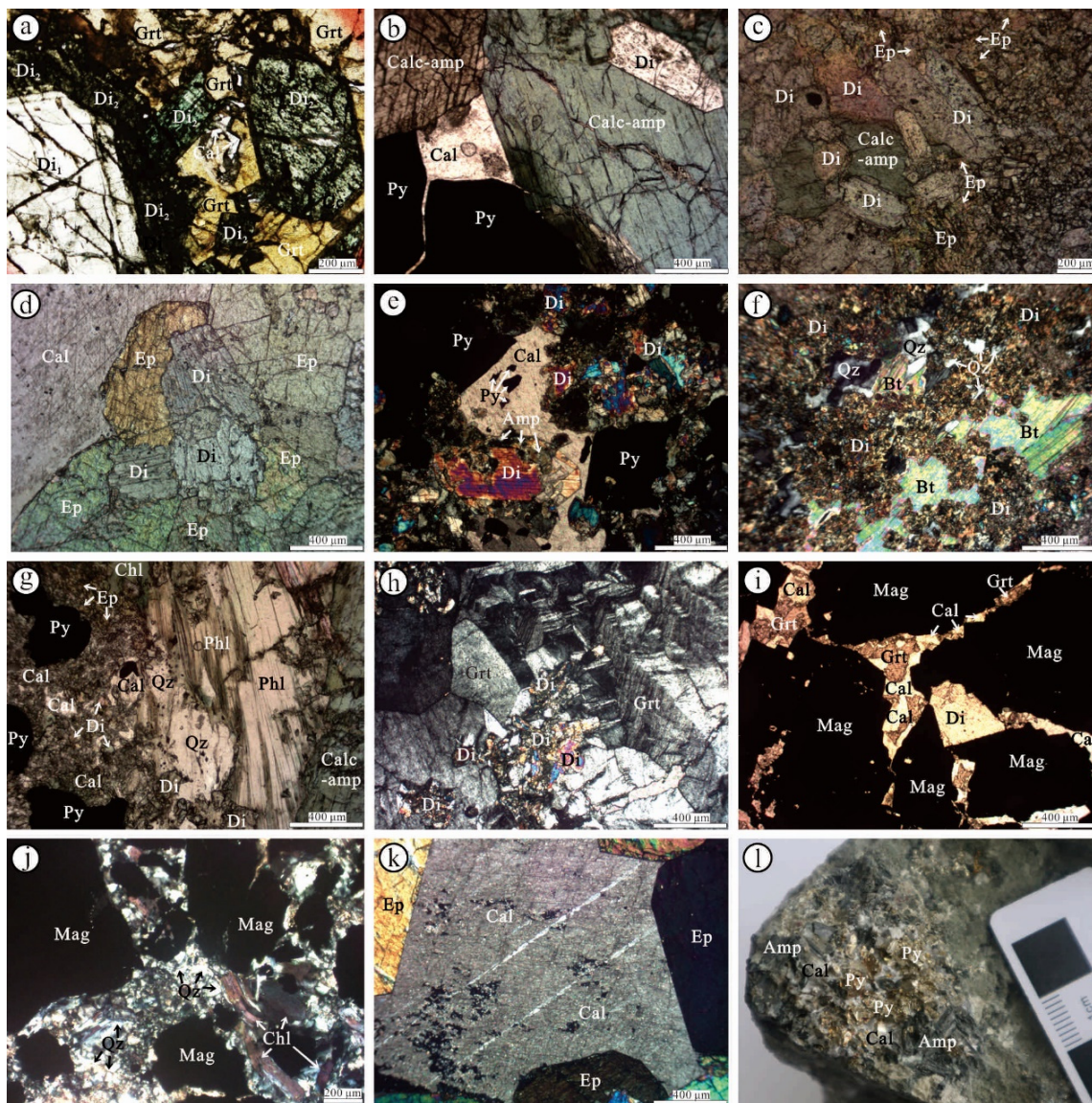


Figure 7. Paragenetic association of minerals from the different stages of mineralization. (a) Two types of euhedral diopside formed during the prograde skarn stage. Light-green diopside, which coexisted with garnet, grew along the margins of the colorless diopside. (b) Subhedral–euhedral Ca-rich amphibole that formed during the retrograde skarn stage. The amphibole replaced the early diopside and was partially replaced by late pyrite and calcite. (c,d) Diopside was replaced by late amphibole and epidote. (e) Early diopside was replaced by late amphibole, both of which were subsequently partially replaced by late pyrite and calcite. (f) Anhedral diopside was metasomatized and partially replaced by biotite and quartz. (g) Epidote, phlogopite, chlorite, calcite, and quartz have partially replaced early diopside. Note the association of phlogopite with Ca-rich amphibole. (h) Diopside was replaced by zoned andradite. (i) Massive magnetite was partially replaced by calcite that was modified by earlier diopside and garnet. (j) Massive magnetite was partially replaced by late anhedral quartz. (k) Euhedral epidote was partially replaced by late anhedral calcite, within which twin lamellae are parallel to the angle bisector of the two heterotropic cleavages. (l) Pyrite associated with calcite that partially replaced euhedral amphibole. Photos (a–d,g,i) were taken under open polarizer, and (e,f,h,j,k) were taken under crossed polarizers. in the figure caption. Abbreviations: Amp = amphibole, Bt = biotite, Calc-amp = calcic amphibole, Cal = calcite, Chl = chlorite, Di = diopside, Di1 = colourless diopside, Di2 = light green diopside, Ep = epidote, Grt = garnet, Mag = magnetite, Phl = phlogopite, Py = pyrite, Qz = quartz.

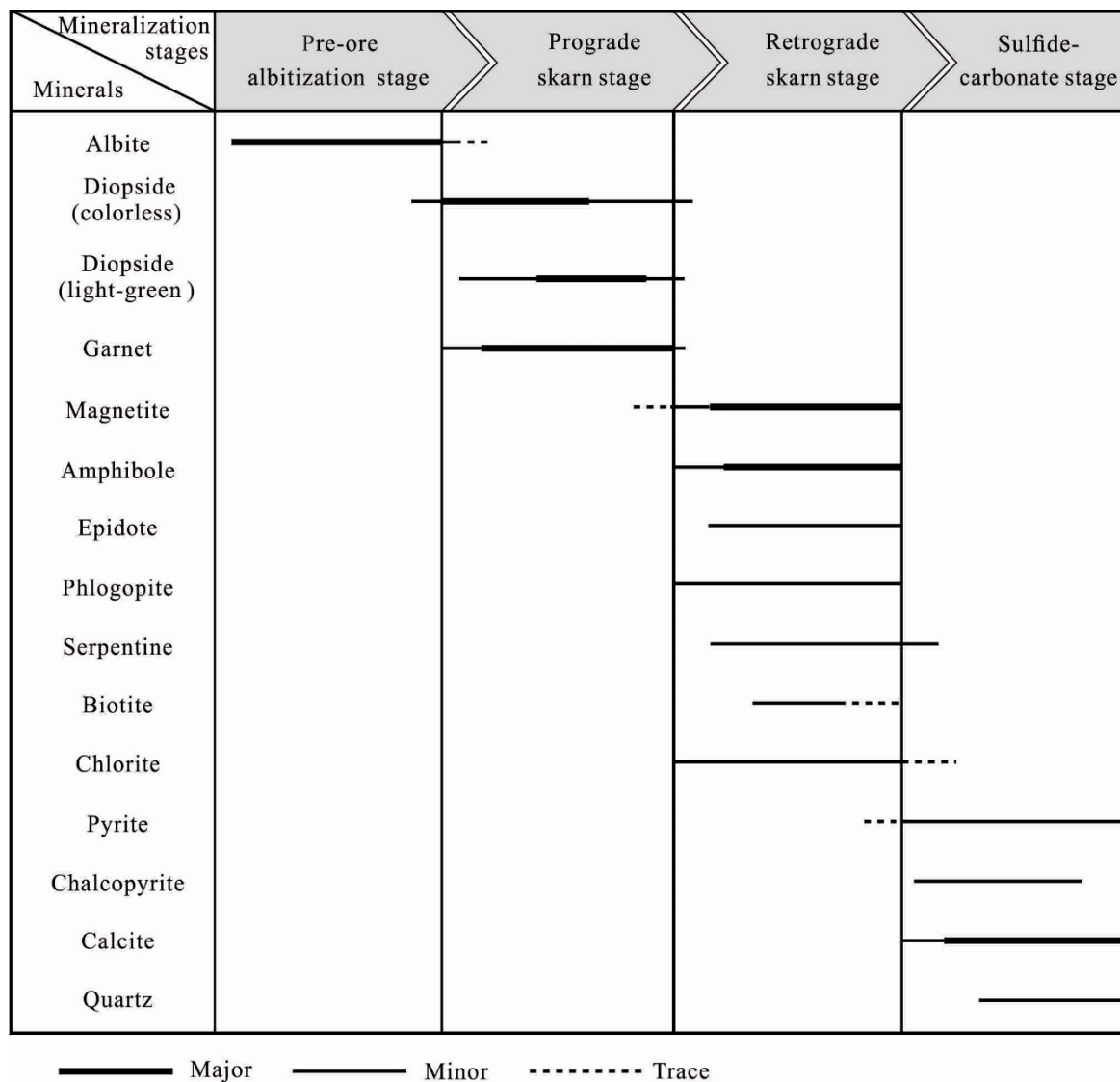


Figure 8. Mineral paragenesis for the Jinling iron skarn deposit.

4. Analytical Methods

Chemical analyses of representative magmatic and mineralized skarn minerals were performed at the Key Laboratory of Mineral Resources Evaluation in Northeast Asia, Jilin University, China. Mineral chemical analyses were carried out by using an electron microprobe analyzer (EMPA, JXA-8200, JEOL produced in Showajima, Tokyo, Japan) with five wavelength-dispersive spectrometers. Natural and synthetic minerals, glass, and pure oxides were taken as standards. Counting times were the 20 s at the peak and in the background. The applied acceleration voltage was 15 kV, the beam current was 10 nA, and the beam diameter for all analyses was typically 2–5 μm. ZAF-correction calculation was carried out during the quantitative analysis.

5. Analytical Results

5.1. Feldspar and Clinopyroxene in the Jinling Diorites

Chemical compositions of representative magmatic feldspar and clinopyroxene from Jinling diorites are presented in Table 1 and Supplementary Table S1.

Table 1. EPMA data for magmatic feldspar from Jinling diorites.

Sample No.	JL-fsp1	JL-fsp2	JL-fsp3	JL-fsp4	JL-fsp5	JL-fsp6	JL-fsp7	JL-fsp8
SiO ₂	67.13	66.46	61.03	67.64	61.71	64.06	64.21	67.91
TiO ₂	0.00	0.00	0.07	0.00	0.00	0.00	0.00	0.04
Al ₂ O ₃	19.15	20.23	23.61	19.62	23.44	18.47	20.69	19.05
Cr ₂ O ₃	0.01	0.00	0.03	0.00	0.00	0.00	0.03	0.00
FeO	0.11	0.03	0.50	0.07	0.48	0.10	0.44	0.04
MnO	0.00	0.05	0.06	0.00	0.06	0.00	0.01	0.00
MgO	0.02	0.07	0.50	0.01	0.29	0.00	0.22	0.00
CaO	0.17	0.09	0.15	0.18	0.24	0.05	0.23	0.09
Na ₂ O	11.32	10.49	7.33	10.84	8.11	4.84	7.48	11.36
K ₂ O	0.09	0.81	3.86	0.66	3.69	11.17	4.91	0.06
Total	98.00	98.23	97.14	99.02	98.02	98.69	98.22	98.55
Si	2.99	2.96	2.79	2.99	2.80	2.97	2.91	3.01
Ti	0.00	0.00	0.00	0.00	0.00	0.00	0.00	0.00
Al	1.01	1.06	1.27	1.02	1.25	1.01	1.11	0.99
Cr	0.00	0.00	0.00	0.00	0.00	0.00	0.00	0.00
Fe ²⁺	0.00	0.00	0.02	0.00	0.02	0.00	0.02	0.00
Mn	0.00	0.00	0.00	0.00	0.00	0.00	0.00	0.00
Mg	0.00	0.01	0.03	0.00	0.02	0.00	0.02	0.00
Ca	0.01	0.00	0.01	0.01	0.01	0.00	0.01	0.00
Na	0.98	0.91	0.65	0.93	0.71	0.44	0.66	0.98
K	0.01	0.05	0.23	0.04	0.21	0.66	0.28	0.00
Total	5.00	4.99	5.00	4.98	5.03	5.08	5.00	4.99
An	0.82	0.45	0.83	0.88	1.25	0.22	1.16	0.41
Ab	98.68	94.74	73.64	95.33	75.98	39.61	69.01	99.24
Or	0.50	4.80	25.53	3.79	22.77	60.17	29.82	0.35

The feldspars are characterized by high Na₂O (4.84 wt.%–11.36 wt.%), low CaO (0.05 wt.%–0.24 wt.%), and highly variable K₂O (0.06 wt.%–11.17 wt.%). Lower total wt.% (ca. 98 wt.%) is due to albitization (Figure 5a). Numbers of cations based on 8 O. They range in composition from 0.22 wt.% to 1.25 wt.% An, 39.61 wt.% to 99.24 wt.% Ab, and 0.35 wt.% to 60.17 wt.% Or. Plagioclase and alkali feldspar are both albitized, with the latter being more intensely altered. In addition, both of these minerals exhibit compositional changes from the core to the rim (Figure 9a), with the alkali feldspar having higher Or and lower An content in the core than the rim (Figure 9b).

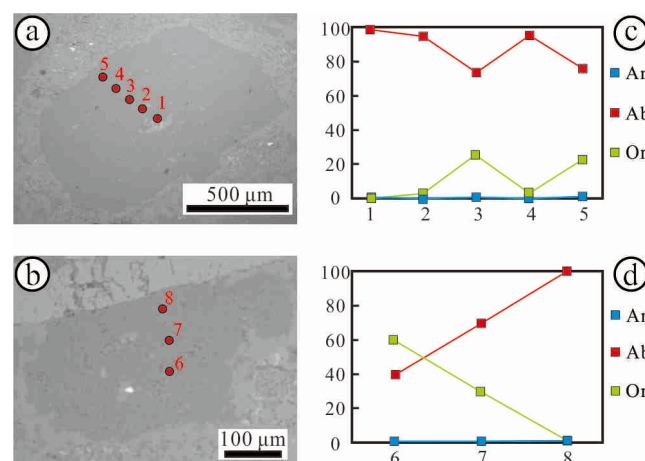


Figure 9. BSE images (a,b) and compositional (c,d) variation of feldspars from Jinling diorites.

The clinopyroxenes exhibit a compositional range of 43.27 wt.%–45.04 wt.% Wo, 42.33 wt.%–44.12 wt.% En, 9.62 wt.%–11.47 wt.% Fs, and 1.14 wt.%–2.02 wt.% Ac (Table 2). In the pyroxene classification ternary diagram, the clinopyroxene samples are plotted in the transitional region between diopside and augite (Figure 10a).

Table 2. Average composition and compositional range of EPMA data for clinopyroxenes from Jinling diorites (JL-cpx1–4), skarn, and ore (JL-cpx5–54, samples JL-cpx5–36 are colorless and samples JL-cpx37–54 are light-green in the Figure 7a).

Sample No.	JL-cpx1–4		JL-cpx5–35		JL-cpx36–54	
	Range (n = 4)	Ave	Range (n = 31)	Ave	Range (n = 19)	Ave
SiO ₂	52.71–54.35	53.51	49.51–56.56	54.08	48.44–54.37	52.84
TiO ₂	0.07–0.32	0.16	0.00–0.13	0.03	0.00–0.19	0.12
Al ₂ O ₃	0.39–1.15	0.66	0.16–5.33	1.16	0.45–5.45	1.31
Cr ₂ O ₃	0.00–0.04	0.02	0.00–0.15	0.02	0.00–0.11	0.03
FeO	5.81–6.96	6.54	0.26–4.51	2.16	6.10–10.23	7.67
MnO	0.21–0.42	0.33	0.00–0.26	0.07	0.15–0.40	0.23
MgO	15.00–15.76	15.45	14.09–18.54	16.93	10.19–14.48	13.40
CaO	21.36–22.52	21.90	24.54–26.22	25.30	22.65–24.56	23.68
Na ₂ O	0.31–0.56	0.42	0.00–0.24	0.10	0.15–0.86	0.50
K ₂ O	0.00–0.01	0.00	0.00–0.04	0.02	0.00–0.12	0.02
Total	98.49–99.64	98.98	98.22–102.64	99.86	98.24–101.34	99.80
Si	1.97–2.01	2.00	1.85–2.01	1.97	1.87–2.01	1.97
Ti	0.00–0.01	0.00	0.00	0.00	0.00–0.01	0.00
IVAl	0.00–0.03	0.01	0.00–0.15	0.03	0.00–0.13	0.03
VIAl	0.02	0.02	0.00–0.09	0.02	0.01–0.11	0.03
Cr	0.00	0.00	0.00	0.00	0.00	0.00
Fe ³⁺	0.00–0.04	0.01	0.00–0.10	0.03	0.00–0.10	0.04
Fe ²⁺	0.17–0.21	0.19	0.00–0.11	0.04	0.14–0.27	0.20
Mn	0.01	0.01	0.00–0.01	0.00	0.00–0.01	0.01
Mg	0.84–0.88	0.86	0.79–1.00	0.92	0.59–0.80	0.75
Ca	0.86–0.89	0.88	0.96–1.01	0.99	0.91–0.99	0.95
Na	0.02–0.04	0.03	0.00–0.02	0.01	0.01–0.06	0.04
K	0.00	0.00	0.00	0.00	0.00–0.01	0.00
Total	3.98–4.03	4.00	3.98–4.05	4.01	3.99–4.04	4.01
Wo	43.27–45.04	44.22	48.49–51.88	49.85	45.65–50.05	47.96
En	42.33–44.12	43.41	40.48–49.93	46.36	30.54–40.31	37.74
Fs	9.62–11.47	10.83	0.39–7.31	3.44	9.74–17.34	12.47
Ac	1.14–2.02	1.54	0.1–0.87	0.35	0.54–3.14	1.83
Di	79.00–83.00	81.25	88.00–100.00	95.39	71.00–84.00	78.33
Hd	16.00–20.00	18.00	0.00–12.00	4.32	15.00–28.00	20.94
Jo	1.00	1.00	0.00–1.00	0.13	1.00	0.94

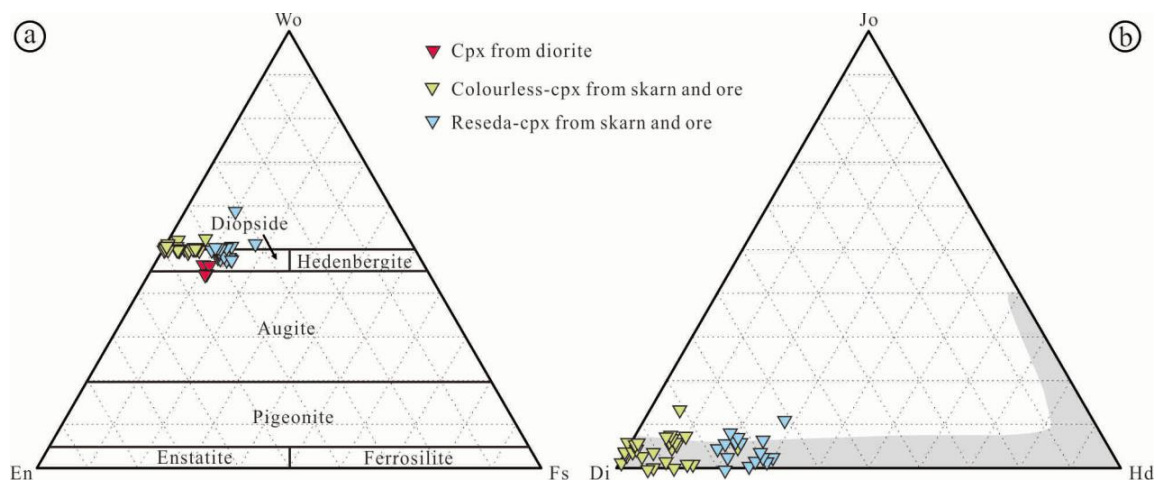


Figure 10. Classification diagram of clinopyroxenes from Jinling diorites, skarn, and ore (a), modified from Morimoto et al. [24]) and the compositional fields for garnet in Fe skarn deposits (Meinert et al. [25]) are shown in the diagram for comparison (b).

5.2. Clinopyroxene, Garnet, and Amphibole in Skarn and Iron Ore

The clinopyroxene from skarn and ores of Jinling iron skarn deposit can be divided into two types of colorless and light green according to the different petrographic characteristics. Chemical compositions of these two types of clinopyroxene are reported in Supplementary Table S1. The numbers of cations based on 6 O and cations are normalized to four in total. The colorless clinopyroxenes in the Jinling iron skarn have a compositional range of 48.49 wt.%–51.88 wt.% Wo, 40.48 wt.%–49.93 wt.% En, 0.39 wt.%–7.31 wt.% Fs, 0.1 wt.%–1.87 wt.% Ac, 0.88 wt.%–1.00 wt.% Di, 0 wt.%–0.12 wt.% Hd, and 0 wt.%–0.01 wt.% Jo. The light-green clinopyroxenes have a compositional range of 45.65 wt.%–50.05 wt.% Wo, 30.54 wt.%–40.31 wt.% En, 9.74 wt.%–17.34 wt.% Fs, 0.54 wt.%–3.14 wt.% Ac, 0.71 wt.%–0.84 wt.% Di, 0.15 wt.%–0.28 wt.% Hd, and 0.01 wt.% Jo. Although the light-green clinopyroxenes have higher FeO and lower MgO and CaO content than the colorless variety, all of the clinopyroxenes are classified as diopside (Figure 10a) and are plotted largely in the iron skarn compositional field on a Jo–Di–Hd discrimination diagram (Figure 10b).

Garnets in the skarn exhibit weak core-to-rim zoning (Figures 7h and 11a). The compositional ranges of the cores (n = 17 spots) and rims (n = 5 spots) were summarized (Table 3). The numbers based on the basis of 12 O and cations are normalized to eight in total. The calculation of Fe²⁺ and Fe³⁺ was completed with the AX program [26]. High total wt.% of garnet including 103 wt.% at max may be related to the selection of standard sample and/or the working status of the instrument. The cores of the garnets range in composition from 90.78 wt.% to 99.57 wt.% Adr, 0.00 wt.% to 8.19 wt.% Grs, and 0.30 wt.% to 2.21 wt.% (Alm + Prp + Sps), whereas the rims range from 61.06 wt.% to 68.49 wt.% Adr, 30.78 wt.% to 38.16 wt.% Grs, and 0.44 wt.% to 0.78 wt.% Alm + Prp + Sps. The rims of the garnets are enriched in Al and depleted in Fe compared with the cores (Figure 11c,d). These compositional relationships are similar to those observed in garnets from other Fe skarn deposits worldwide (Figure 11b).

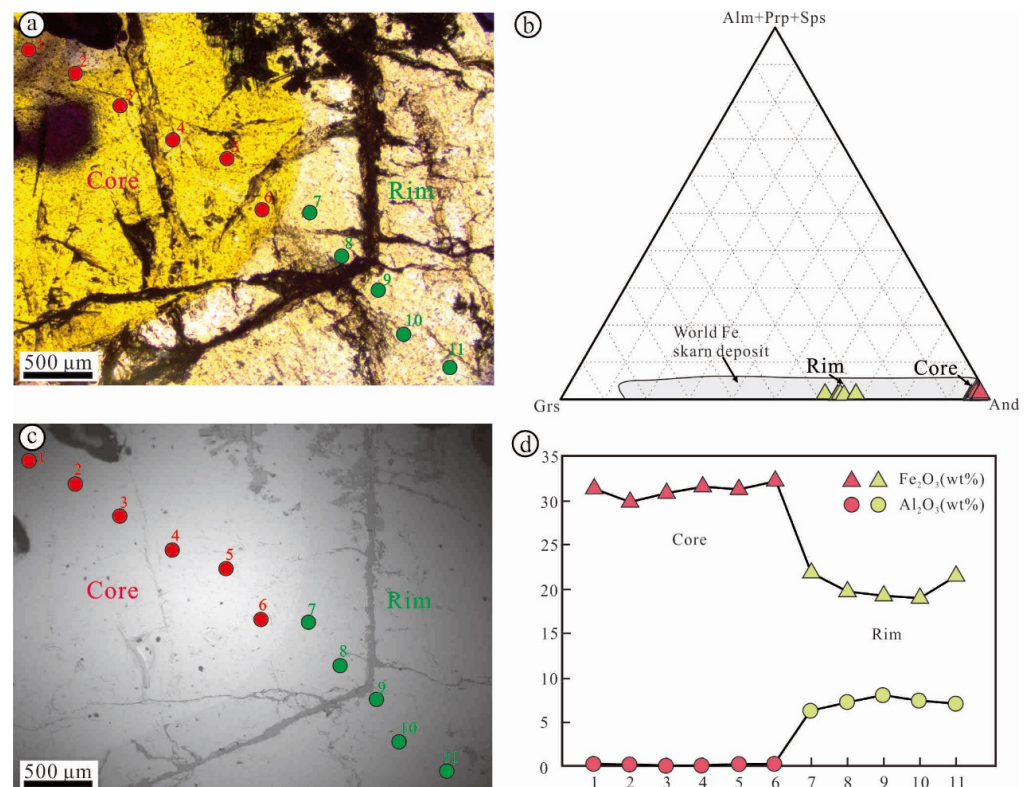


Figure 11. Photomicrographs were taken under open polarizer (a), BSE image (c) and compositional variation (b,d) of garnets from Jinling skarn and ore and the compositional fields for garnet in Fe skarn deposits (Meinert et al. [25]) are shown in the diagram for comparison.

Table 3. EPMA data for garnets from skarn and ore Jinling deposit (JL-grt7–11 from the rim and others from the core).

Sample No.	JL-grt1	JL-grt2	JL-grt3	JL-grt4	JL-grt5	JL-grt6	JL-grt7	JL-grt8	JL-grt9	JL-grt10	JL-grt11
SiO ₂	35.80	36.90	36.45	36.32	36.69	36.41	37.58	37.98	37.35	38.03	37.54
Al ₂ O ₃	0.18	0.20	0.08	0.10	0.22	0.28	6.26	7.28	8.02	7.41	7.06
TiO ₂	0.00	0.01	0.00	0.00	0.00	0.00	0.16	0.04	0.00	0.05	0.00
Fe ₂ O ₃	31.53	30.08	31.10	31.75	31.47	32.47	22.12	19.90	19.24	19.13	21.58
FeO	0.29	1.61	1.11	0.53	0.69	0.30	0.38	1.07	0.62	1.69	0.20
MnO	0.12	0.11	0.10	0.09	0.10	0.16	0.26	0.25	0.25	0.08	0.12
MgO	0.01	0.03	0.01	0.03	0.02	0.02	0.02	0.00	0.00	0.00	0.03
CaO	33.16	33.04	32.96	33.18	33.55	33.39	34.43	34.17	34.18	34.08	34.75
Na ₂ O	0.02	0.01	0.03	0.05	0.01	0.05	0.03	0.06	0.00	0.02	0.04
K ₂ O	0.00	0.00	0.00	0.01	0.00	0.03	0.04	0.02	0.00	0.00	0.01
Cr ₂ O ₃	0.00	0.01	0.01	0.03	0.03	0.00	0.02	0.00	0.07	0.00	0.04
Total	101.12	101.99	101.86	102.08	102.78	103.09	101.29	100.77	99.72	100.49	101.36
Si	3.00	3.05	3.03	3.01	3.02	2.99	3.03	3.06	3.03	3.07	3.01
Ti	0.00	0.00	0.00	0.00	0.00	0.00	0.01	0.00	0.00	0.00	0.00
Al	0.02	0.02	0.01	0.01	0.02	0.03	0.59	0.69	0.77	0.71	0.67
Cr	0.00	0.00	0.00	0.00	0.00	0.00	0.00	0.00	0.00	0.00	0.00
Fe ³⁺	1.99	1.87	1.94	1.98	1.95	2.01	1.34	1.21	1.17	1.16	1.30
Fe ²⁺	0.02	0.11	0.08	0.04	0.05	0.02	0.03	0.07	0.04	0.11	0.01
Mn	0.01	0.01	0.01	0.01	0.01	0.01	0.02	0.02	0.02	0.01	0.01
Mg	0.00	0.00	0.00	0.00	0.00	0.00	0.00	0.00	0.00	0.00	0.00
Ca	2.97	2.93	2.93	2.95	2.96	2.94	2.97	2.95	2.97	2.94	2.99
Na	0.00	0.00	0.00	0.01	0.00	0.01	0.01	0.01	0.00	0.00	0.01
K	0.00	0.00	0.00	0.00	0.00	0.00	0.00	0.00	0.00	0.00	0.00
Total	8.01	8.00	8.00	8.00	8.00	8.00	8.00	8.00	8.00	8.00	8.00
Uv	0.00	0.04	0.04	0.11	0.10	0.00	0.05	0.00	0.21	0.00	0.13
Adr	99.13	98.99	99.57	99.39	98.82	98.64	68.49	64.65	61.06	64.27	65.81
Prp	0.05	0.12	0.04	0.11	0.08	0.06	0.10	0.00	0.00	0.00	0.11
Sps	0.29	0.26	0.25	0.21	0.23	0.37	0.59	0.58	0.57	0.19	0.27
Grs	0.00	0.00	0.00	0.00	0.00	0.00	30.78	34.76	38.16	35.29	33.68
Alm	0.68	0.89	1.38	1.18	0.83	1.74	0.00	0.00	0.00	0.25	0.00

Sample No.	JL-grt12	JL-grt13	JL-grt14	JL-grt15	JL-grt16	JL-grt17	JL-grt18	JL-grt19	JL-grt20	JL-grt21	JL-grt22
SiO ₂	36.96	36.37	38.37	36.17	36.11	36.81	36.41	36.01	36.89	36.84	36.22
Al ₂ O ₃	0.25	1.88	7.65	0.64	0.91	0.40	0.26	0.27	0.24	0.20	0.23
TiO ₂	0.00	0.00	0.04	0.04	0.00	0.00	0.00	0.00	0.00	0.04	0.00
Fe ₂ O ₃	29.97	28.73	19.40	28.97	31.6	30.84	31.59	30.96	30.25	30.25	31.37
FeO	1.09	0.61	2.21	1.13	0.29	0.43	0.29	0.28	1.20	1.07	0.29
MnO	0.08	0.07	0.07	0.08	0.08	0.09	0.04	0.06	0.09	0.13	0.15
MgO	0.01	0.00	0.04	0.04	0.04	0.04	0.06	0.03	0.04	0.09	0.00
CaO	33.57	33.31	33.91	32.60	33.67	33.78	33.85	33.71	33.34	33.10	33.29
Na ₂ O	0.00	0.02	0.02	0.05	0.01	0.03	0.06	0.01	0.00	0.04	0.05
K ₂ O	0.00	0.01	0.01	0.00	0.00	0.00	0.01	0.00	0.01	0.05	0.01
Cr ₂ O ₃	0.02	0.00	0.00	0.14	0.00	0.03	0.03	0.05	0.00	0.05	0.01
Total	101.96	101.00	101.72	99.86	102.71	102.45	102.59	101.39	102.06	101.84	101.60
Si	3.06	3.01	3.06	3.05	2.97	3.03	3.00	3.00	3.05	3.05	3.01
Ti	0.00	0.00	0.00	0.00	0.00	0.00	0.00	0.00	0.00	0.00	0.00
Al	0.02	0.18	0.72	0.06	0.09	0.04	0.03	0.03	0.02	0.02	0.02
Cr	0.00	0.00	0.00	0.01	0.00	0.00	0.00	0.00	0.00	0.00	0.00
Fe ³⁺	1.86	1.79	1.16	1.84	1.96	1.91	1.96	1.94	1.88	1.88	1.96
Fe ²⁺	0.08	0.04	0.15	0.08	0.02	0.03	0.02	0.02	0.08	0.07	0.02
Mn	0.01	0.01	0.01	0.01	0.01	0.01	0.00	0.00	0.01	0.01	0.01
Mg	0.00	0.00	0.01	0.01	0.01	0.01	0.01	0.00	0.01	0.01	0.00
Ca	2.97	2.96	2.90	2.94	2.97	2.98	2.99	3.01	2.95	2.94	2.97
Na	0.00	0.00	0.00	0.01	0.00	0.01	0.01	0.00	0.00	0.01	0.01
K	0.00	0.00	0.00	0.00	0.00	0.00	0.00	0.00	0.00	0.01	0.00
Total	8.00	8.00	8.00	8.00	8.01	8.00	8.01	8.01	8.00	8.00	8.00
Uv	0.07	0.00	0.00	0.46	0.00	0.10	0.10	0.15	0.00	0.15	0.03
Adr	97.64	90.78	63.57	96.32	95.63	97.31	98.65	97.50	98.84	98.86	98.83
Prp	0.05	0.00	0.17	0.16	0.15	0.18	0.26	0.11	0.18	0.36	0.00
Sps	0.18	0.16	0.15	0.18	0.19	0.22	0.09	0.15	0.20	0.30	0.35
Grs	2.05	8.19	34.22	2.47	2.45	2.20	0.78	2.10	0.53	0.12	0.35
Alm	0.00	0.87	1.89	0.42	1.57	0.00	0.12	0.00	0.24	0.20	0.43

Chemical compositions of amphibole from skarn and iron ore are reported in Table 4. F and Cl are below the detection limit. The numbers based on the basis of 23 O and cations are normalized to 16 in total. The calculation of Fe²⁺ and Fe³⁺ was completed by AX program [26]. The grain sizes of amphiboles in skarn and iron ore are 2–8 mm in length. The amphiboles are characterized by high CaO (12.27–12.83 wt.%) and low Na₂O (2.32–3.25 wt.%) content. These amphiboles are classified as pargasite based on their Si (5.54–5.93), Ca_B (1.96–2.02), and (Na + K)_A (0.95–1.06) values (Figure 12) and the fact that ^{VI}Al (0.56–0.81) is greater than or equal to Fe³⁺ (0.42–0.74).

Table 4. EPMA data for amphiboles from Jinling skarn and ore.

Sample No.	JL-amp1	JL-amp2	JL-amp3	JL-amp4	JL-amp5	JL-amp6	JL-amp7	JL-amp8	JL-amp9	JL-amp10	JL-amp11	JL-amp12	JL-amp13	JL-amp14
SiO ₂	39.25	38.35	39.75	37.23	39.68	39.26	38.68	39.62	38.99	38.12	38.18	38.58	38.78	38.42
TiO ₂	0.71	0.43	0.34	0.34	0.37	0.30	0.37	0.23	0.50	0.52	0.40	0.46	0.26	0.22
Al ₂ O ₃	16.29	17.21	15.16	18.27	15.55	15.34	16.71	15.66	15.19	17.50	18.63	17.16	16.50	16.45
Cr ₂ O ₃	0.06	0.02	0.00	0.00	0.08	0.03	0.11	0.00	0.02	0.00	0.00	0.04	0.00	0.00
FeO	8.17	8.40	10.50	8.89	9.11	9.79	8.28	8.49	9.99	8.60	8.09	7.85	8.79	8.63
MnO	0.08	0.11	0.15	0.10	0.04	0.10	0.13	0.09	0.19	0.09	0.05	0.05	0.08	0.13
MgO	14.96	14.48	13.65	14.01	14.47	14.28	14.72	15.13	13.91	14.30	14.22	14.65	14.47	14.44
CaO	12.56	12.51	12.43	12.47	12.62	12.27	12.55	12.68	12.50	12.83	12.76	12.56	12.56	12.54
Na ₂ O	2.46	2.87	2.44	2.99	3.25	2.96	2.69	2.62	2.32	2.93	3.16	2.79	2.64	2.46
K ₂ O	1.44	0.96	1.44	0.59	0.67	0.81	1.18	1.07	1.53	1.01	0.74	1.09	1.42	1.47
Total	95.98	95.34	95.86	94.89	95.84	95.14	95.42	95.59	95.14	95.90	96.23	95.23	95.50	94.76
Si	5.79	5.69	5.93	5.54	5.88	5.86	5.73	5.84	5.84	5.61	5.60	5.72	5.76	5.74
Ti	0.08	0.05	0.04	0.04	0.04	0.03	0.04	0.03	0.06	0.06	0.04	0.05	0.03	0.03
^{IV} Al	2.20	2.31	2.06	2.45	2.13	2.13	2.26	2.13	2.14	2.38	2.40	2.28	2.24	2.25
^{VI} Al	0.64	0.70	0.61	0.76	0.57	0.57	0.66	0.60	0.56	0.67	0.81	0.72	0.64	0.65
Cr	0.007	0.002	0.000	0.000	0.009	0.004	0.013	0.000	0.003	0.000	0.000	0.005	0.000	0.000
Fe ³⁺	0.48	0.53	0.42	0.68	0.43	0.54	0.53	0.63	0.63	0.74	0.50	0.45	0.52	0.66
Fe ²⁺	0.53	0.51	0.89	0.42	0.70	0.68	0.50	0.42	0.62	0.32	0.49	0.52	0.57	0.42
Mn	0.01	0.01	0.02	0.01	0.01	0.01	0.02	0.01	0.02	0.01	0.01	0.01	0.01	0.02
Mg	3.29	3.20	3.04	3.11	3.20	3.18	3.25	3.33	3.11	3.14	3.11	3.24	3.20	3.21
Ca	1.98	1.99	1.99	1.99	2.00	1.96	1.99	2.00	2.01	2.02	2.00	2.00	2.00	2.01
Na	0.70	0.83	0.71	0.86	0.93	0.86	0.77	0.75	0.67	0.84	0.90	0.80	0.76	0.71
K	0.27	0.18	0.27	0.11	0.13	0.15	0.22	0.20	0.29	0.19	0.14	0.21	0.27	0.28
Total	16.04	16.01	15.98	15.97	16.11	16.02	16.11	15.94	15.97	15.96	16.01	16.05	16.01	15.97
Mg/(Mg + Fe ²⁺)	0.86	0.86	0.77	0.88	0.82	0.82	0.87	0.89	0.83	0.91	0.86	0.86	0.85	0.88
Ca _B	1.98	1.99	1.99	1.99	2.00	1.96	1.99	2.00	2.01	2.02	2.00	2.00	2.00	2.01
Na _B	0.02	0.01	0.01	0.01	0.00	0.04	0.01	0.00	0.00	0.00	0.00	0.00	0.00	0.00
Na _A	0.69	0.81	0.69	0.85	0.94	0.82	0.77	0.75	0.68	0.86	0.90	0.80	0.76	0.72
K _A	0.27	0.18	0.27	0.11	0.13	0.15	0.22	0.20	0.29	0.19	0.14	0.21	0.27	0.28

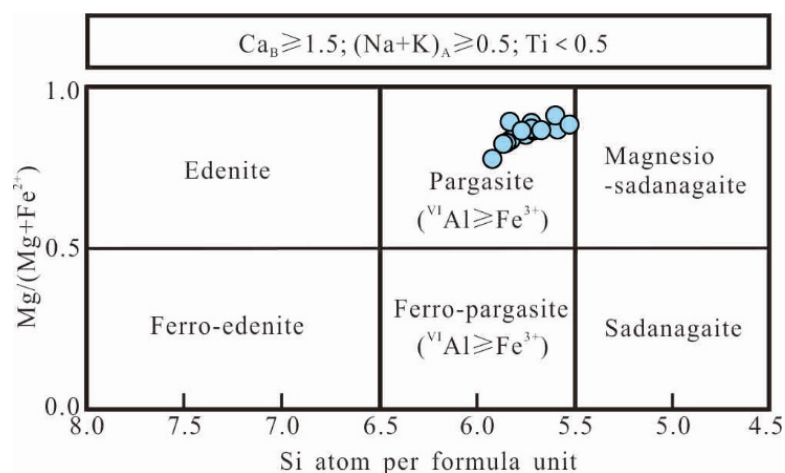


Figure 12. Classification diagram of amphiboles from Jinling skarn and ore.

5.3. Magnetite from Diorite, Skarn, and Iron Ore

The representative compositions of disseminated, banded, and massive magnetite are summarized in Supplementary Table S2. The numbers of cations based on 32 O and cations are normalized to 24 in total. The calculation of Fe²⁺ and Fe³⁺ was completed by the AX program [26]. Disseminated and banded magnetites have FeO, MgO, SiO₂, Al₂O₃, and TiO₂ content of 83.43 wt.%–92.10 wt.%, 0.00 wt.%–7.86 wt.%, 0.03 wt.%–2.57 wt.%,

0.14 wt.%–1.33 wt.%, and 0.00 wt.%–0.87 wt.%, respectively. Massive magnetites are characterized by higher FeO (87.81 wt.%–94.57 wt.%) content and lower MgO (0.01 wt.%–0.60 wt.%), SiO₂ (0.03 wt.%–1.10 wt.%), TiO₂ (0.00 wt.%–0.14 wt.%), and Al₂O₃ (0.00 wt.%–0.45 wt.%) content than the disseminated and banded magnetite (Table 5; Figure 13). Small magnetite crystals in the massive assemblages have higher FeO content than the larger crystals (Figure 13).

Table 5. EPMA data for magnetites from Jinling diorites, skarn, and ore.

Sample No.	JL-mag1–3 Magmatic Magnetite		JL-mag4–10 Disseminated Magnetite		JL-mag11–18 Banded Magnetite		JL-mag19–51 Massive Magnetite	
	Range (n = 3)	Ave	Range (n = 7)	Ave	Range (n = 8)	Ave	Range (n = 33)	Ave
SiO ₂	0.03–0.05	0.04	0.03–2.57	0.87	0.03–0.16	0.08	0.03–1.10	0.31
TiO ₂	0.06–0.27	0.17	0.00–0.18	0.07	0.25–0.87	0.61	0.00–0.14	0.04
Al ₂ O ₃	0.04–0.30	0.13	0.31–1.33	0.56	0.14–1.25	0.70	0.00–0.45	0.18
Cr ₂ O ₃	0.75–0.88	0.81	0.00–0.07	0.02	0.00–0.12	0.03	0.00–1.57	0.07
V ₂ O ₃	0.36–1.03	0.77	0.02–0.07	0.04	0.00–0.07	0.02	0.00–0.07	0.02
FeO	89.89–90.84	90.42	86.40–92.10	90.16	83.43–88.59	85.75	87.81–94.57	92.05
MnO	0.00–0.03	0.01	0.00–0.10	0.03	0.14–0.36	0.23	0.00–0.16	0.05
MgO	0.00–0.03	0.02	0.00–1.03	0.30	3.54–7.86	5.95	0.01–0.60	0.15
CaO	0.00–0.07	0.03	0.00–1.21	0.38	0.00	0.00	0.00–0.32	0.04
Total	91.69–92.82	92.41	91.64–93.14	92.43	91.90–94.26	93.36	89.37–95.29	92.91
Si	0.01	0.01	0.01–0.78	0.27	0.01–0.05	0.02	0.01–0.35	0.09
Ti	0.01–0.06	0.04	0.00–0.04	0.02	0.06–0.19	0.13	0.00–0.03	0.01
Al	0.01–0.11	0.05	0.11–0.48	0.20	0.05–0.42	0.24	0.00–0.16	0.06
Cr	0.18–0.22	0.20	0.00–0.02	0.01	0.00–0.03	0.01	0.00–0.39	0.02
V	0.09–0.26	0.19	0.00–0.01	0.01	0.00–0.02	0.01	0.00–0.02	0.00
Fe ³⁺	15.42–15.49	15.45	13.90–15.85	15.22	15.17–15.82	15.44	15.20–15.94	15.71
Fe ²⁺	8.01–8.06	8.03	7.94–8.05	8.02	4.76–6.48	5.52	7.77–8.29	8.01
Mn	0.00–0.01	0.00	0.00–0.03	0.01	0.03–0.09	0.06	0.00–0.04	0.01
Mg	0.00–0.02	0.01	0.00–0.47	0.14	1.57–3.35	2.58	0.01–0.28	0.07
Ca	0.00–0.02	0.01	0.00–0.39	0.12	0.00	0.00	0.00–0.11	0.01
Total	24.00	24.00	24.00	24.00	24.00	24.00	24.00	24.00
V/Ti	0.00–0.02	0.01	0.29–15.36	6.67	0.00–0.17	0.06	0.00–3.21	0.65

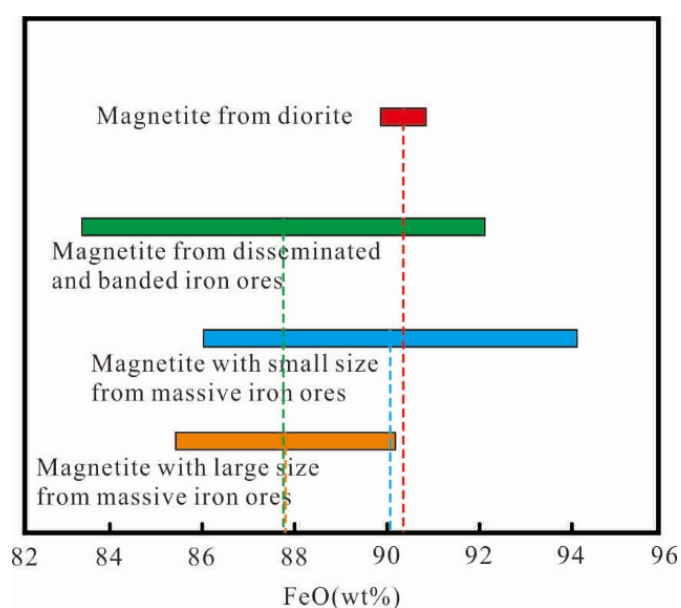


Figure 13. Variation in FeO content from magmatic, disseminated, banded, and massive magnetites from Jinling diorites, skarn, and ore.

6. Discussion

6.1. Source of Iron

Previous studies have suggested two potential sources of iron for the iron skarn mineralization: (1) exsolution of Fe-rich fluids from silicate melt at depth, and (2) leaching of Fe from sedimentary wall rocks and the solidified mafic pluton at relatively shallow depths [27]. Several earlier studies addressed that the magma from which the Jinling diorites crystallized most probably originated from mixing between enriched mantle-derived mafic magma and felsic magma derived from the ancient lower crust of the NCC [7,9,28]. Because the mantle-derived magma had relatively high Fe content and the ancient crust of the NCC comprised mafic rocks and BIFs, the parental magma of the Jinling diorites would also have contained relatively high iron content, which is in agreement with the high FeO content (89.89 wt.%–90.84 wt.%) of the magmatic magnetite in the diorites (Table 5). Furthermore, given the high fO_2 of the melt (+0.83~+1.87 [29]), sulfur likely existed as SO_4^{2-} rather than S^{2-} , and therefore Fe would not have been removed by sulfide liquation. Consequently, Fe would have remained in the silicate melt until reaching fluid saturation. This view is supported by experimental and fluid-inclusion studies that demonstrated the high solubility of Fe (>10 wt.%) as iron chloride complexes in high-temperature and high-salinity magmatic fluids [30,31]. The presence of halite-bearing fluid inclusions in quartz that crystallized during the later stages of formation of the Jinling diorites [32] suggests that the hydrothermal fluids were Cl-rich and might have had the potential to transport Fe. Therefore, the parent magma of the Jinling intrusion was characterized by high iron content along with high oxygen fugacity, which favored the retention of metallogenic material in the melt. Fluid exsolution occurred when the melt reached water saturation as a result of decreases in temperature and pressure during magma ascent, emplacement, and fractionation. Concurrently, more iron entered the fluids and formed the iron-rich ore-forming fluids.

Alkali metal ions are considered an important complexing agent for Fe and can contribute to the emigration of Fe from silicate melts or minerals [33]. The importance of such ions as complexing agents in the Jinling diorite is supported by the pervasive alkali metasomatism (mainly albitization) (Figures 5a–c and 9a,b). The magmatic clinopyroxene in the Jinling diorites is plotted in the transitional region between diopside and augite on a clinopyroxene classification diagram (Figure 10a), indicating that Fe was remobilized from augite to diopside by the hydrothermal fluids. The metasomatism also affected plagioclase, alkali feldspar, and mafic minerals, further augmenting the Fe content of the hydrothermal fluid. Given that the carbonate wall rocks do not contain significant concentrations of Fe, they could not have been a source of the Fe. Therefore, the most likely scenario in which the Fe skarn mineralization formed in the Jinling deposit was the leaching of Fe from the solidified diorites by Fe-rich magmatic fluids derived from the primitive melt.

Magmatic and hydrothermal magnetite are compositionally distinct, with the former being enriched in such elements as Ti and V [34]. This characteristic can therefore be used to deduce the nature (i.e., magmatic vs. hydrothermal) of skarn mineralization [35,36]. Two models have been proposed for the genesis of magnetite in iron skarn deposits: (1) crystallization from an immiscible Fe-rich melt that exsolved from the parent magma [37] and (2) precipitation from hydrothermal fluids [38,39]. Genetic classification diagrams, such as Ti vs. (Ni/Cr) and (Al + Mn) vs. (Ti + V) diagrams, cannot be utilized to accurately distinguish between magmatic magnetite from volcanic rocks and hydrothermal magnetite from skarn, porphyry, Ag–Pb–Zn, or bedded Cu–Ag deposits [40]. The origins of magnetite can, however, be characterized using a Fe vs. (V/Ti) classification diagram, which was proposed based on the compatibility of these elements in magnetite and the disparity in the concentrations of these elements in silicate melts and hydrothermal fluids [40]. In an Fe vs. (V/Ti) diagram, the magnetite in the Jinling iron ores is plotted mainly in the hydrothermal magnetite field, with some in the re-equilibrated magnetite field (Figure 14). This suggests that the magnetite in the Jinling iron ores is hydrothermal in origin. In addition, the disseminated, banded, and massive magnetite in the Jinling iron ores are all

characterized by low TiO_2 and V_2O_3 content (0.01 wt.%–0.87 wt.% and 0.01 wt.%–0.07 wt.%, respectively) (Table 5), typical of hydrothermal magnetite [34,41]. Combined with the fact that the ore bodies hosted in the contact zone underwent intense metasomatism and are distributed close to the wall rocks, the Jinling iron skarn deposit can be characterized as a hydrothermal skarn deposit.

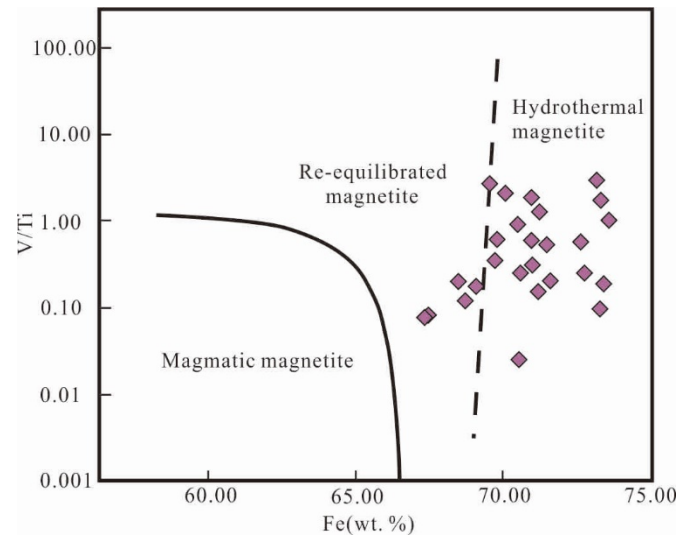


Figure 14. Fe vs. V/Ti genetic type discrimination diagram for magnetites from the skarn and ore of the Jinling deposit (modified from Wen [40]).

6.2. Implications for Mineralization Processes

6.2.1. Alkali Metasomatism Stage

During the alkali metasomatism stage, iron was added to the hydrothermal fluid via fluid–mineral interaction. This interaction generated the pervasive alkali metasomatism in the Jinling diorites and magmatic minerals, such as plagioclase, alkali feldspar, amphibole, and pyroxene, in them (Figures 5a–c and 9a,b).

6.2.2. Prograde Skarn Stage

The mineral assemblage diopside–andradite \pm disseminated and banded magnetite formed during the prograde skarn stage. The paragenesis of skarn minerals, combined with variations in their chemical composition, can be used to characterize the physicochemical conditions of the ore-forming fluids and the processes that generate iron mineralization. The hydrothermal fluids migrated from the Jinling pluton to the surrounding carbonate rocks owing to differences in the physicochemical conditions during the emplacement and crystallization of the pluton. Calcium and magnesium were continuously added to the hydrothermal fluids by the metamorphically induced decomposition and recrystallization of the carbonate rocks. This increase in Ca and Mg concentrations allowed high-temperature Ca- and Mg-rich skarn minerals (i.e., diopside and garnet) to crystallize as fluid temperatures decreased. Previous studies have demonstrated that the breakdown of carbonate minerals and the subsequent extraction of Ca^{2+} and Mg^{2+} are accelerated under acidic and reducing conditions [42]. Therefore, the crystallization of Ca–Mg-bearing diopside and andradite suggests that the hydrothermal fluid that exsolved from the parental magma was relatively acidic and weakly reducing. The light-green diopside is characterized by higher FeO and lower MgO and CaO content than the earlier colorless variety (i.e., the clinopyroxenes vary from diopside to hedenbergite) (Table 2; Figure 10), suggesting that the redox conditions of the hydrothermal fluid evolved from relatively reducing to relatively oxidizing as the concentration of an iron ion in the fluid increased.

Previous research suggests that skarn-related garnets can crystallize over a range of redox conditions, which is recorded in their iron and aluminum content. Consequently, the

composition of garnet can be used as a proxy for changing redox conditions in hydrothermal fluids [43]. In addition, experimental results suggest that andradite typically forms under alkaline and oxidizing conditions, whereas grossular garnet typically forms under acidic and reducing conditions [44]. Andradite from the Jinling skarn is compositionally zoned, with higher Fe_2O_3 and lower Al_2O_3 in cores than rims (Figure 11). Furthermore, the cores of the andradite are characterized by a wider range in And (cores: 63.57 wt.%–99.57 wt.% vs. rims: 61.06 wt.%–68.49 wt.%) and Gro (cores: 0.00 wt.%–8.19 wt.% vs. rims: 30.78 wt.%–38.16 wt.%) content than the rims (Table 3). This, again, suggests that the redox conditions of the hydrothermal fluid evolved from relatively oxidizing to relatively reducing. However, the chemical compositions of the cores and rims of garnet are characterized by low $\text{Fe}^{2+}/\text{Fe}^{3+}$ values (0.01–0.13). Given that the $\text{Fe}^{2+}/\text{Fe}^{3+}$ values of skarn minerals formed under reducing conditions are higher than those formed under oxidizing conditions [45], the relative oxidizing conditions of the mineralizing environment during the prograde skarn stage can be constrained with minor changes.

As mentioned above, the colorless diopside formed earlier under relative reduction conditions, but the later light-green diopside and coextensive andradite crystallized under relative oxidation conditions. The redox conditions evolved from relatively reducing earlier to relatively oxidizing later during the entire prograde skarn stage, despite changing slightly during the formation of andradite. The model of ironstone formation from modern hydrothermal settings indicates that the Fe^{2+} ions can migrate from the reducing hydrothermal environment to the relatively oxidizing surface layer [4]. Meanwhile, given that Fe is more soluble in hydrothermal fluids under alkaline and oxidizing conditions than under reducing conditions [46], it is likely that Fe was further enriched in the ore-forming fluids under the relative oxidizing conditions during the later prograde skarn stage.

Diopside crystallizes at temperatures and pressures greater than 520 °C and 2 kbar [47], whereas andradite crystallizes within a temperature range of 300–520 °C and at pressures of around 0.5 kbar [48]. In the Jinling iron skarn deposit, colorless diopside formed earlier than both light-green diopside and andradite, suggesting that the temperature and pressure of the hydrothermal system decreased during the prograde skarn stage. Consequently, fluid boiling likely occurred once hydrostatic pressure equaled the saturation pressure [49]. The occurrence of fluid boiling is supported by (i) the abrupt changes in FeO and Al_2O_3 content from core to rim of andradite (Figure 11), and (ii) evidence from fluid-inclusion microthermometry, which suggests that the fluids boiled at temperatures above 500–600 °C [32]. Owing to gas loss during boiling, Fe concentrations and the pH of the hydrothermal fluid increased, prompting the dissociation of iron chloride complexes, which caused the precipitation of magnetite near the boiling surface [50]. Hence, a small amount of disseminated and banded magnetite formed during the prograde skarn stage.

6.2.3. Retrograde Skarn Stage

The amphibole–epidote–phlogopite–serpentine–biotite–chlorite–massive magnetite association was developed during the retrograde skarn stage. Diopside and garnet formed earlier and were subsequently substituted by massive magnetite coexisting with biotite, chlorite, and serpentine (Figures 6g–j and 7i), whereas Ca-rich amphibole associated with phlogopite or epidote was replaced by later pyrite or calcite (Figure 7b,c,e).

Previous studies have demonstrated that an increase in $f\text{O}_2$ not only decreases the partition coefficient of V into magnetite but also promotes the formation of epidote [35,51]. Therefore, the lower V content of massive magnetite (0.01 wt.%–0.05 wt.%) compared with disseminated and banded magnetite (0.01 wt.%–0.70 wt.%) (Table 5), together with the occurrence of epidote, suggest that this stage was characterized by higher $f\text{O}_2$ and pH than the prograde skarn stage. Furthermore, under such alkaline conditions, the hydrothermal fluid might have leached Fe from other minerals [52], which is consistent with the negative correlation between FeO and MgO or Al_2O_3 of magnetite in the Jinling ore (Figure 15). As the temperature of the hydrothermal fluid decreased, the solubility of Si, Al, Mg, and Ca also decreased, prompting the precipitation of hydrous minerals, such as phlogopite,

epidote, amphibole, and chlorite, under conditions of decreasing temperature and pressure, high oxygen fugacity and alkalinity, and iron-enriched fluids. This view is supported by the higher FeO content of massive magnetite (87.81 wt.%–94.57 wt.%) than disseminated and banded magnetite (83.43 wt.%–92.10 wt.%) (Table 5), and similarly high FeO content of epidote (12.40 wt.%–13.87 wt.%) (Table 6; numbers of cations based on 12.5 O and cations are normalized to eight in total). As a result of these courses mentioned above, the concentration of iron in the hydrothermal fluids would have been further enriched during the early retrograde skarn stage.

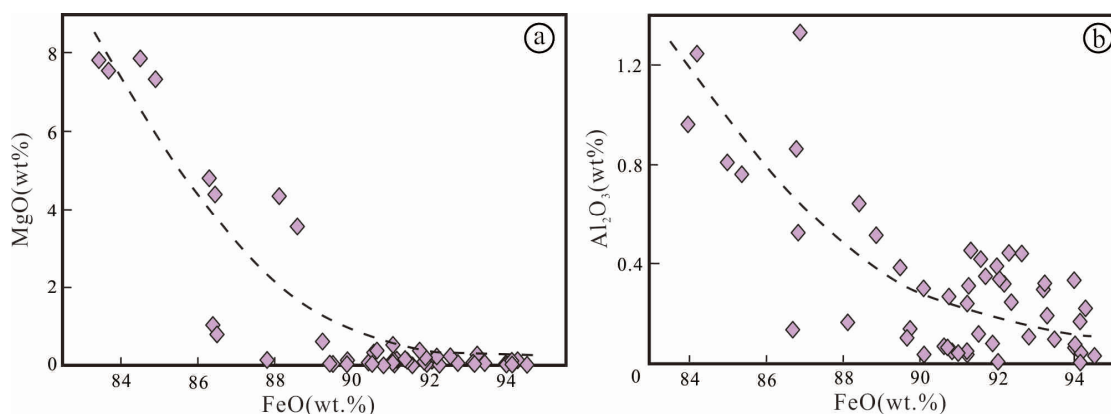


Figure 15. FeO vs. MgO diagram (a) and FeO vs. Al₂O₃ diagram (b) for magnetites from the skarn and ore of the Jinling deposit.

Table 6. EPMA data for epidote from Jinling skarn and ore.

	Range (<i>n</i> = 10)	Ave		Range (<i>n</i> = 10)	Ave
SiO ₂	37.43–38.09	37.79	Si	3.00–3.04	3.03
TiO ₂	0.00–0.42	0.13	Al	0.00–0.03	0.01
Al ₂ O ₃	21.32–22.72	21.96	Ti	2.02–2.14	2.07
Cr ₂ O ₃	0.00–0.07	0.01	Cr	0.00	0.00
Fe ₂ O ₃	13.78–15.41	14.65	Fe ³⁺	0.83–0.93	0.87
MnO	0.00–0.11	0.06	Mn	0.00–0.01	0.00
MgO	0.00–0.05	0.03	Mg	0.00–0.01	0.00
CaO	22.82–23.51	23.05	Ca	1.96–2.01	1.98
Na ₂ O	0.00–0.14	0.06	Na	0.00–0.02	0.01
K ₂ O	0.00–0.02	0.01	K	0.00	0.00
Total	97.31–98.42	97.75	Total	7.98–8.01	7.99

Stable isotope and fluid-inclusion data from the skarn deposit suggest that the ore-forming fluids of the retrograde skarn stage would be mixed with meteoric water [42]. The nonuniform distribution of oxygen isotopes in epidote from the Jinling skarn [32] suggests that the ore-forming fluids were mixed with fluids from other sources. Upon reaching Fe saturation, the oxygen fugacity and pH of the ore-forming fluids increased rapidly [53], which destabilized the iron chloride complexes and reduced the solubility of Fe [54]. This prompted the rapid precipitation of magnetite, forming the high-grade massive magnetite ores.

6.2.4. Sulfide–Carbonate Stage

During the sulfide–carbonate stage, abundant carbonate minerals (mostly calcite) and minor sulfides (e.g., pyrite and chalcopyrite) and quartz formed interstitial to skarn minerals (Figures 6i,j and 7a–f,i–l). Pyrite also formed as late-stage veins that cut the iron ore (Figure 6k,l). The precipitation of abundant magnetite caused the redox conditions of the mineralizing fluid to become more reducing, which is consistent with the growth of sulfide minerals.

6.2.5. Summary of Mineralization Processes

The mineralizing processes of the Jinling iron skarn deposit can be summarized in four stages. (1) During the alkali metasomatism stage, hydrothermal fluids exsolved from an Fe-rich parental magma and concentrated Fe by leaching it from the solidified diorite pluton (Figure 16a). (2) During the prograde skarn stage, high-temperature, anhydrous skarn minerals (diopside + garnet) formed as a result of fluid–rock interaction. Iron was further enriched in the fluids under the relatively oxidizing and alkaline conditions. A decrease in pressure during the later period of this stage caused the fluid to boil and locally precipitate small amounts of disseminated and banded magnetite (Figure 16b). (3) During the retrograde skarn stage, a decrease in temperature and pressure and a rise in the fO_2 of the hydrothermal fluid prompted the precipitation of hydrous, low-temperature skarn minerals (amphibole + chlorite + epidote). Iron was further enriched during this stage as a result of this precipitation. The precipitation of large quantities of magnetite was initiated by the mixing of the ore-forming fluids with fluids from other sources (e.g., meteoric fluids) (Figure 16c). (4) During the sulfide–carbonate stage, large quantities of carbonate and small amounts of sulfides and quartz precipitated as the redox conditions of the hydrothermal fluid became reducing (Figure 16d).

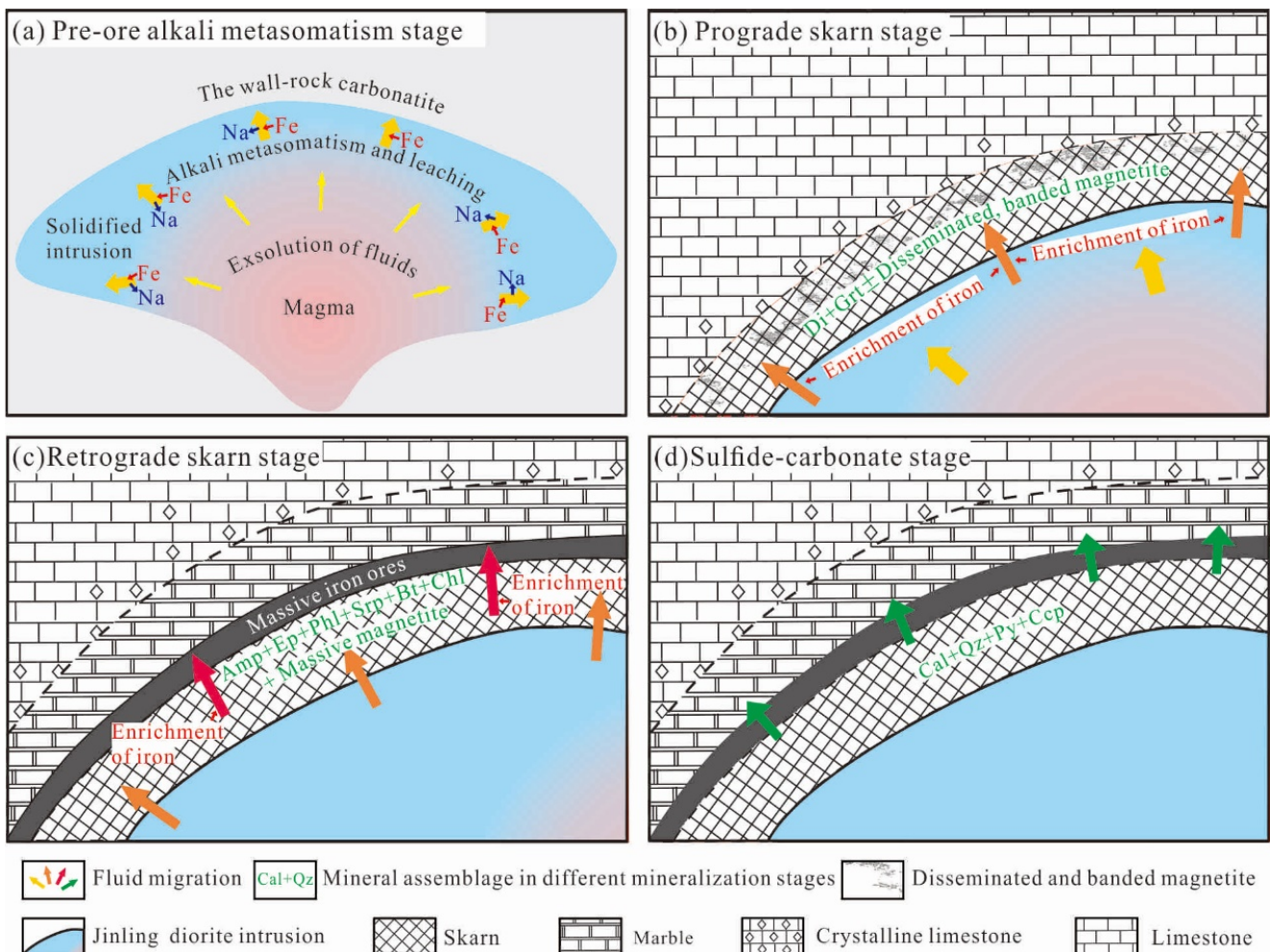


Figure 16. Sketch model of mineralizing processes of the Jinling deposit, Western Shandong Province. (a) Alkali metasomatism stage along with fluid exsolution. (b) Diopside and garnet formed due to fluid–rock interaction during the prograde skarn stage. (c) Amphibole, chlorite and epidote formed and the precipitation of large quantities of magnetite occurred during the retrograde skarn stage. (d) Carbonate, quartz and small amounts of sulfides formed during the sulfide–carbonate stage.

7. Conclusions

The Jinling deposit is a hydrothermal iron skarn deposit. The Fe-rich mineralizing fluids exsolved from the parental magma and were further enriched by Fe leached from the solidified diorites. As part of the mineralizing process, high-temperature anhydrous skarn minerals (diopside + garnet) formed during the prograde skarn stage under relatively oxidizing and alkaline conditions, whereas low-temperature hydrous skarn minerals (amphibole + chlorite + epidote) formed during the retrograde skarn stage under more oxidizing conditions. Large quantities of massive magnetite precipitated during the later retrograde skarn stage as a result of mixing between the mineralizing fluids and fluids from other sources. Then, the redox conditions became more reducing during the sulfide-carbonate stage, and large quantities of carbonate and small amounts of sulfides and quartz precipitated.

Supplementary Materials: The following supporting information can be downloaded at: <https://www.mdpi.com/article/10.3390/min12091152/s1>, Table S1. EPMA data for clinopyroxenes from Jinling diorites (JL-cpx1-4), skarn and ore (JL-cpx5-54, samples JL-cpx5-35 are colorless and samples JL-cpx36-54 are light-green); Table S2. EPMA data for magnetites from Jinling diorites, skarn and ore.

Author Contributions: Conceptualization, F.-H.C., C.Z. and J.-L.G.; data curation, D.-T.J. and L.-Y.W.; formal analysis, M.M. and Y.-D.L.; funding acquisition, F.-H.C. and J.-L.G.; methodology, C.Z., L.-Y.W. and J.-L.G.; project administration, F.-H.C.; software, D.-T.J. and L.-Y.W.; validation, L.-Y.W. and J.-L.G.; writing—original draft, F.-H.C. and C.Z.; writing—review and editing, F.-H.C., C.Z. All authors have read and agreed to the published version of the manuscript.

Funding: This research was funded by the Science Foundation of Shandong Province (ZR2021MD104, ZR2019PD010, ZR2016DB08), Science and Technology Research Project of Shandong Bureau of Geology and Mineral Resources (KY202201, KC201901), and the Opening Foundation of Key Laboratory of Mineral Resources Evaluation in Northeast Asia, Ministry of Land and Resources (DBY-KF-19-15).

Data Availability Statement: Not applicable.

Acknowledgments: We acknowledge the detailed comments of anonymous journal reviewers.

Conflicts of Interest: The authors declare no conflict of interest.

References

1. Dill, H.G. The “chessboard” classification scheme of mineral deposits: Mineralogy and geology from aluminum to zirconium. *Earth Sci. Rev.* **2010**, *100*, 1–420. [[CrossRef](#)]
2. Zhao, Y.M.; Feng, C.Y.; Li, D.X. New progress in prospecting for skarn deposits and spatial-temporal distribution of skarn deposits in China. *Mineral Deposits*. **2017**, *36*, 519–543. (In Chinese with English abstract)
3. Burkhalter, R.M. Ooidal ironstones and ferruginous microbialites: Origin and relation to sequence stratigraphy (Aalenian and Bajocian, Swiss Jura mountains). *Sedimentology* **1995**, *42*, 57–74. [[CrossRef](#)]
4. Di Bella, M.; Sabatino, G.; Quartieri, S.; Ferretti, A.; Cavalazzi, B.; Barbieri, R.; Foucher, F.; Messori, F.; Italiano, F. Modern Iron Ooids of Hydrothermal Origin as a Proxy for Ancient Deposits. *Sci. Rep.* **2019**, *9*, 7107. [[CrossRef](#)]
5. Zhao, G.C.; Cawood, P.A.; Li, S.Z.; Wilde, S.A.; Sun, M.; Zhang, J.; He, Y.H.; Yin, C.Q. Amalgamation of the North China Craton: Key issues and discussion. *Precambrian Res.* **2012**, *222–223*, 55–76. [[CrossRef](#)]
6. Zhang, S.H.; Zhao, Y.; Davis, G.A.; Ye, H.; Wu, F. Temporal and spatial variations of Mesozoic magmatism and deformation in the North China Craton: Implications for lithospheric thinning and decratonization. *Earth Sci. Rev.* **2014**, *131*, 49–87.
7. Shen, J.F.; Santosh, M.; Li, S.R.; Zhang, H.F.; Yin, N.; Dong, G.C.; Wang, Y.J.; Ma, G.G.; Yu, H.J. The Beiminghe skarn iron deposit, eastern China: Geochronology, isotope geochemistry and implications for the destruction of the North China Craton. *Lithos* **2013**, *156–159*, 218–229. [[CrossRef](#)]
8. Deng, X.D.; Li, J.W.; Wen, G. Dating iron skarn mineralization using hydrothermal allanite-(La) U–Th–Pb isotopes by laser ablation ICP-MS. *Chem. Geol.* **2014**, *382*, 95–110. [[CrossRef](#)]
9. Duan, Z.; Li, J.W. Zircon and titanite U–Pb dating of the Zhangjiawa iron skarn deposit, Luxi district, North China Craton: Implications for a craton-wide iron skarn mineralization. *Ore Geol. Rev.* **2017**, *89*, 309–323. [[CrossRef](#)]
10. Xie, Q.H.; Zhang, Z.C.; Jin, Z.L.; Santosh, M.; Han, L.; Wang, K.Y.; Zhao, P.L.; He, H.H. The high-grade Fe skarn deposit of Jinling, North China Craton: Insights into hydrothermal iron mineralization. *Ore Geol. Rev.* **2021**, *138*, 104395. [[CrossRef](#)]
11. Jin, Z.L.; Zhang, Z.C.; Hou, T.; Santosh, M.; Han, L. Genetic relationship of high-Mg dioritic pluton to iron mineralization: A case study from the Jinling skarn-type iron deposit in the North China Craton. *J. Asian Earth Sci.* **2015**, *113*, 957–979. [[CrossRef](#)]

12. Shen, J.F.; Li, S.R.; Santosh, M.; Dong, G.C.; Wang, Y.J.; Liu, H.M.; Peng, Z.D.; Zhang, Z.Y. Zircon U–Pb geochronology of the basement rocks and dioritic intrusion associated with the Fushan skarn iron deposit, southern Taihang Mountains, China. *J. Asian Earth Sci.* **2015**, *113*, 1132–1142. [[CrossRef](#)]
13. Xie, Q.H.; Zhang, Z.C.; Hou, T.; Santosh, N.; Jin, Z.L.; Liu, H.; Cheng, Z.G. Petrogenesis of the Zhangmatun gabbro in the Ji’nan complex, North China Craton: Implications for skarn-type iron mineralization. *J. Asian Earth Sci.* **2015**, *113*, 1197–1217. [[CrossRef](#)]
14. Zhu, B.; Zhang, H.F.; Zhao, X.M.; He, Y.S. Iron isotope fractionation during skarn-type alteration: Implications for metal source in the Han-Xing iron skarn deposit. *Ore Geol. Rev.* **2016**, *74*, 139–150. [[CrossRef](#)]
15. Zhang, X.; Yang, X.Y.; Pirajno, F. Recycling of Paleo-Pacific subducted oceanic crust related to a Fe–Cu–Au mineralization in the Xu-Huai region of North Anhui-Jiangsu, East China: Geochronological and geochemical constraints. *Int. Geol. Rev.* **2012**, *60*, 1–23.
16. Chen, Y.J.; Su, S.G.; He, Y.S.; Li, S.G.; Hou, J.G.; Feng, S.C.; Gao, K. Fe isotope compositions and implications on mineralization of Xishimen iron deposit in Wuan, Hebei. *Acta Petrol. Sin.* **2014**, *30*, 3443–3454, (In Chinese with English abstract).
17. Zhao, J.S.; Zhao, B.; Li, J.W.; Xu, D.R.; He, M.C.; Zheng, J.P. Magma control of magmatic skarn to the formation of some deposits of skarn type: Evidence from Laser Raman analyses of inclusions in minerals. *Acta Petrol. Sin.* **2015**, *31*, 1079–1088. (In Chinese with English abstract)
18. Zhao, G.; Zhai, M. Lithotectonic elements of Precambrian basement in the North China Craton: Review and tectonic implications. *Gondwana Res.* **2013**, *23*, 1207–1240. [[CrossRef](#)]
19. Yang, Q.; Santosh, M. Paleoproterozoic arc magmatism in the North China Craton: No Siderian global plate tectonic shutdown. *Gondwana Res.* **2015**, *28*, 82–105. [[CrossRef](#)]
20. Zhao, G.C.; Sun, M.; Wilde, S.A.; Li, S.Z. Late Archean to Paleoproterozoic evolution of the North China Craton: Key issues revisited. *Precambrian Res.* **2005**, *136*, 177–202. [[CrossRef](#)]
21. Zhai, M.G.; Santosh, M. The early Precambrian odyssey of the North China Craton: A synoptic overview. *Gondwana Res.* **2011**, *20*, 6–25. [[CrossRef](#)]
22. Lan, T.G.; Fan, H.R.; Hu, F.F.; Tomkins, A.; Yang, K.F.; Liu, Y.S. Multiple crust-mantle interactions for the destruction of the North China Craton: Geochemical and Sr-Nd-Pb-Hf isotopic evidence from the Longbaoshan alkaline complex. *Lithos* **2011**, *122*, 87–106. [[CrossRef](#)]
23. Hao, X.Z. Study on Metallogenic Regularities and Prognosis of Iron Deposits in Western Shandong Province. Ph.D. Thesis, China University of Geosciences, Wuhan, China, 2014; pp. 1–197. (In Chinese with English abstract)
24. Morimoto, N.; Fabries, J.; Ferguson, A.K.; Ginzburg, I.V.; Ross, M.; Seifert, F.A.; Zussman, J.; Aoki, K.; Gottardi, G. Nomenclature of pyroxenes. *Am. Mineral.* **1988**, *73*, 1123–1133.
25. Meinert, L.D.; Dipple, G.M.; Nicolescu, S. World Skarn Deposits. In *Economic Geology 100th Anniversary Volume*; GeoScienceWorld: McLean, VA, USA, 2005; pp. 299–336.
26. Wang, S.L.; Wang, G.H.; Du, J.X.; Zhao, J.; Chen, Y.X.; Xiu, D. Petrology and metamorphic P-T path of the garnet amphibolite in the Wenquan Group, western North Tianshan, China. *Acta. Petrol. Sin.* **2018**, *34*, 3658–3670. (In Chinese with English abstract)
27. Zhao, Y.M.; Lin, W.W.; Bi, C.S.; Li, D.X. Basic geological characteristics of skarn deposits of China. *Bull. Chin. Acad. Geol. Sci.* **1986**, *14*, 59–87. (In Chinese)
28. Lan, T.G.; Hu, R.Z.; Chen, Y.H.; Wang, H.; Tang, Y.W.; Liu, L. Generation of high-Mg diorites and associated iron mineralization within an intracontinental setting: Insights from ore-barren and ore-bearing intrusions in the eastern North China Craton. *Gondwana Res.* **2019**, *72*, 97–119. [[CrossRef](#)]
29. Zhang, C.; Cui, F.H.; Geng, R.; Zhang, Z.L.; Gao, M.B.; Gao, J.L. The petrogenesis of early Cretaceous Quartz diorite in skarn iron deposits, Jinling area, Luxi: Evidence of geochronology and geochemistry. *Miner. Petrol.* **2021**, *41*, 80–92. (In Chinese with English abstract)
30. Heinrich, C.A.; Günther, D.; Audétat, A.; Ulrich, T.; Frischknecht, R. Metal fractionation between magmatic brine and vapor, determined by microanalysis of fluid inclusions. *Geology* **1999**, *27*, 755. [[CrossRef](#)]
31. Ulrich, T.; Gunther, D.; Heinrich, C.A. The Evolution of a porphyry Cu-Au deposit, based on LA-ICP-MS analysis of fluid inclusions: Bajo de la Alumbrera, Argentina. *Econ. Geol.* **2002**, *97*, 1889–1920. [[CrossRef](#)]
32. Jin, Z.L. Genesis of High-Grade Fe Skarns: A Case Study of Zibo and Laiwu Iron Deposits in Western Shandong. Ph.D. Thesis, China University of Geosciences, Wuhan, China, 2017; pp. 1–120. (In Chinese with English abstract)
33. Kwak, T.A.P.; Brown, W.M.; Abeyasinghe, P.B.; Tan, T.H. Fe solubilities in very saline hydrothermal fluids: Their relation to zoning in some ore deposits. *Econ. Geol.* **1986**, *81*, 447–465. [[CrossRef](#)]
34. Hu, H.; Li, J.W.; Lentz, D.; Ren, Z.; Zhao, X.F.; Deng, X.D.; Hall, D. Dissolution-reprecipitation process of magnetite from the Chengchao iron deposit: Insights into ore genesis and implication for in-situ chemical analysis of magnetite. *Ore Geol. Rev.* **2014**, *57*, 393–405. [[CrossRef](#)]
35. Nadoll, P.; Angerer, T.; Mauk, J.L.; French, D.; Walshe, J. The chemistry of hydrothermal magnetite: A review. *Ore Geol. Rev.* **2014**, *61*, 1–32. [[CrossRef](#)]
36. Knipping, J.L.; Bilenker, L.D.; Simon, A.C.; Reich, M.; Barra, F.; Deditius, A.P.; Wälle, M.; Heinrich, C.A.; Holtz, F.; Munizaga, R. Trace elements in magnetite from massive iron oxide-apatite deposits indicate a combined formation by igneous and magmatic-hydrothermal processes. *Geochim. Cosmochim. Acta* **2015**, *171*, 15–38. [[CrossRef](#)]
37. Tang, P.Z.; Wang, J.B.; Wang, Y.W.; Long, L.L. Geochemical characteristics of mafic-ultramafic rocks in the Cihai ore district, Xinjiang, and their geological significance. *Geochimica* **2010**, *39*, 542–552. (In Chinese with English abstract)

38. Hou, T.; Zhang, Z.C.; Santosh, M.; Encarnacion, J.; Wang, M. The Cihai diabase in the Beishan region, NW China: Isotope geochronology, geochemistry and implications for Cornwall-style iron mineralization. *J. Asian Earth Sci.* **2013**, *70*, 231–249. [[CrossRef](#)]
39. Huang, X.W.; Zhou, M.F.; Qi, L.; Gao, J.F.; Wang, Y.W. Re-Os isotopic ages of pyrite and chemical composition of magnetite from the Cihai magmatic-hydrothermal Fe deposit, NW China. *Miner. Deposita* **2013**, *48*, 925–946. [[CrossRef](#)]
40. Wen, G.; Li, J.W.; Hofstra, A.H.; Koenig, A.E.; Lowers, H.A.; Adams, D. Hydrothermal reequilibration of igneous magnetite in altered granitic plutons and its implications for magnetite classification schemes: Insights from the Handan-Xingtai iron district, North China Craton. *Geochim. Cosmochim. Acta* **2017**, *213*, 255–270. [[CrossRef](#)]
41. Pang, K.N.; Zhou, M.F.; Lindsley, D.; Zhao, D.; Malpas, J. Origin of Fe-Ti Oxide Ores in Mafic Intrusions: Evidence from the Panzhihua Intrusion, SW China. *J. Petrol.* **2008**, *49*, 295–313. [[CrossRef](#)]
42. Zhao, Y.M.; Lin, W.W. *Skarn Deposits of China*; Geological Publishing House: Beijing, China, 2012; pp. 1–354. (In Chinese with English abstract)
43. Jamtveit, B.; Wogelius, R.A.; Fraser, D.G. Zonation patterns of skarn garnets: Records of hydrothermal system evolution. *Geology* **1993**, *21*, 113–116. [[CrossRef](#)]
44. Ai, Y.F.; Jin, L.N. The study of the relationship between the mineralization and the garnet in the skarn ore deposits. *Acta Sci. Nat. Univ. Pekin.* **1981**, *1*, 83–90. (In Chinese with English abstract)
45. Zaw, K.; Singoyi, B. Formation of magnetite-scheelite skarn mineralization at Kara, Northwestern Tasmania: Evidence from mineral chemistry and stable isotopes. *Econ. Geol.* **2000**, *95*, 1215–1230. [[CrossRef](#)]
46. Liang, X.J. Garnets of grossular-andradite series: Their characteristics and metasomatic mechanism. *Acta Petrol. Miner.* **1994**, *13*, 342–352. (In Chinese with English abstract)
47. Einaudi, M.T.; Meinert, L.D.; Newberry, R.J. Skarn Deposits. In *Economic Geology 75th Anniversary Volume*; Economic Geology Publishing: Littleton, CO, USA, 1981; pp. 317–391.
48. Einaudi, M.T.; Burt, D.M. Introduction-terminology, classification and composition of skarn deposits. *Econ. Geol.* **1982**, *77*, 745–754. [[CrossRef](#)]
49. Yardley, B.W.D.; Rochelle, C.A.; Barnicoat, A.C. Oscillatory zoning in metamorphic minerals: An indicator of infiltration metasomatism. *Mineral. Mag.* **1991**, *55*, 357–365. [[CrossRef](#)]
50. Brimhall, G.H.; Crerar, D.A. Ore fluids: Magmatic to supergene. In *Thermodynamic Modeling of Geological Materials: Minerals, Fluids and Melts*; Carmichael, I.S.E., Eugster, H.P., Eds.; De Gruyter: Berlin/Heidelberg, Germany, 1987; Volume 17, pp. 235–321.
51. Perkins, E.H.; Brown, T.H.; Berman, R.G. PTX-SYSTEM: Three programs for calculation of pressure-temperature-composition phase diagrams. *Comput. Geosci.* **1987**, *12*, 749–755. [[CrossRef](#)]
52. Hong, W.; Zhang, Z.H.; Zhao, J.; Wang, Z.H.; Li, F.M.; Shi, F.P.; Liu, X.Z. Mineralogy of the Chagangnuoer iron deposit in Western Tianshan Mountains, Xinjiang, and its geological significance. *Acta Petrol. Miner.* **2012**, *31*, 191–211. (In Chinese with English abstract)
53. Zhang, D.H. Some new advances in ore-forming fluid geochemistry on boiling and mixing of fluids during the processes of hydrothermal deposits. *Adv. Earth Sci.* **1997**, *12*, 49–55. (In Chinese with English abstract).
54. Whitney, J.A.; Hemley, J.J.; Simon, F.O. The concent ratio of iron in chloride solutions equilibrated with synthetic granitic compositions; the sulfur-free system. *Econ. Geol.* **1985**, *80*, 444–460. [[CrossRef](#)]